

Data-constrained analytical model for the propagation of a penny-shaped hydraulic fracture under true triaxial stresses

Runhua Feng (✉ runhua.feng@student.curtin.edu.au)

Curtin University <https://orcid.org/0000-0003-1722-4265>

Joel Sarout

CSIRO Kensington: CSIRO Australian Resources Research Centre

Jeremie Dautriat

CSIRO Kensington: CSIRO Australian Resources Research Centre

Jiecheng Zhang

Peking University School of Earth and Space Sciences

Hamid Roshan

UNSW: University of New South Wales

Reza Rezaee

Curtin University - Perth Bentley Campus: Curtin University

Mohammad Sarmadivaleh

Curtin University Bentley Campus: Curtin University

Research Article

Keywords: Temporal radius prediction, Penny-shaped hydraulic fracture, Linear elastic fracture growth, Tip asymptotic solutions, Poiseuille's law, Self-similar propagation

Posted Date: July 15th, 2022

DOI: <https://doi.org/10.21203/rs.3.rs-1525036/v3>

License: © ⓘ This work is licensed under a Creative Commons Attribution 4.0 International License.

[Read Full License](#)

Data-constrained analytical model for the propagation of a penny-shaped hydraulic fracture under true triaxial stresses

Runhua Feng^{1*}, Joel Sarout², Jeremie Dautriat², Jiecheng Zhang³, Hamid Roshan⁴, Reza Rezaee¹, Mohammad Sarmadivaleh¹

¹School of WASM: Minerals, Energy and Chemical Engineering, Curtin University, 26 Dick Perry Ave, Kensington, WA 6151 Australia

²CSIRO Energy, Perth, WA 6151, Australia

³Beijing International Center for Gas Hydrate, School of Earth and Space Sciences, Peking University, Beijing 100871, China

⁴School of Minerals and Energy Resources Engineering, UNSW AUSTRALIA, Kensington, Sydney 2052, Australia

*Corresponding author:

E-mail address: runhua.feng@student.curtin.edu.au (R.Feng)

Highlights:

- An analytical model (R_d) based on Poiseuille's law and self-similar growth is developed to predict the temporal radius of a penny-shaped hydraulic fracture under stable or unstable propagation cases. The prediction based on linear elastic model (R_E); and tip asymptotic solutions are also used as comparison.
- The applicability of asymptotic solutions is restricted to linearly elastic homogeneous materials, i.e. PMMA. The performance of linear elastic model R_E poorly agree with the experimental data, especially for unstable propagation cases.
- The model R_d takes advantage of a fast reconstruction of the temporal radius of a penny-shaped hydraulic fracture under more realistic conditions, i.e., multiscale propagation regimes, cohesive effects, stable or unstable propagation in different geomaterials.

Abstract

Hydraulic fracturing is a coupled multi-physics and scale-dependent process requiring an extensive numerical-laboratory appraisal to assess feasibility in the field. Developing a robust model of hydraulic fracture propagation requires knowledge of the time evolution of the fracture's geometrical attributes, e.g., width/aperture and length/radius. However, it is inherently challenging to directly measure even the simplest fracture attribute (i.e., radius) within a rock sample subjected to *in-situ* stresses in the laboratory, let alone in the field. In this study, an analytical model is developed to predict the time evolution of the radius for a penny-shaped hydraulic fracture. This model (R_d) predicts the fracture opening and internal pressure gradient using Poiseuille's law and assuming a self-similar propagation. Scaling laws and dimensional analysis are used to define propagation regimes; and non-linear hydro-mechanical coupling is accounted for in the near-tip region. We also quantify the growth of the fracture radius using linear elastic fracture growth model (R_E); and tip asymptotic solutions (R_V and R_T). A comparison of the three analytical models with published experimental data reveal that (i) the asymptotic solutions are limited to linearly elastic and homogeneous materials, i.e., PMMA; (ii) the performance of the linear elastic model (R_E) poorly matches the experimental data, especially for unstable propagation situations; (iii) the new R_d model takes advantage of a robust reconstruction of the temporal radius growth of hydraulic fracture problems under realistic stress conditions, and including multiscale propagation regimes, cohesive effects, as well as stable and unstable propagation regimes of geomaterials.

Keywords: Temporal radius prediction; Penny-shaped hydraulic fracture; Linear elastic fracture growth; Tip asymptotic solutions; Poiseuille's law; Self-similar propagation

1. Introduction

Fluid-driven fracture propagation has been extensively studied for application to subsurface reservoir stimulation operations (Bunger 2005; Adachi et al. 2007; Sarmadivaleh 2012; Lecampion et al. 2017; Garagash 2019; Feng et al. 2020; Zeng et al. 2020; Huang and Chen 2021), geothermal energy extraction (Legartha et al. 2005; Ranjith et al. 2012; Shao et al. 2015), CO₂ geo-sequestration (Papanastasiou et al. 2016), control of fluid-induced seismicity (Amitrano 2003; Shapiro 2015), and modelling of magma migration (Weinberg and Regenauer-Lieb 2010). The underlying hydro-mechanical interactions taking place at depth are

governed by the coupling between fluid flow and rock deformation under prescribed *in-situ* stress conditions.

Early investigations of crack propagation in solids were based on mathematical solutions of elasticity, i.e., solving integral equations (England and Green 1963; Green and Zerna 1992), or using the Fourier transform (Sneddon 1946; Sneddon 1995). In the initial attempts, mathematical solutions were proposed for the propagation of a Griffith fracture in plane strain (Sneddon and Elliot 1946), and for the propagation of a penny-shaped fracture in three dimensions (Sneddon 1946).

Later, these models were enriched to account for fluid flow, fluid mass balance and fracture geometry, and applied to hydraulic fracturing problems, e.g., (i) Perkins and Kern (1961) and Nordgren (1972) developed the so-called PKN model for the propagation in the horizontal direction of a vertical fracture with an elliptical cross-section, assuming a constant fracture height much smaller than fracture length, and a one-dimensional fluid flow within the fracture; (ii) Zheltov (1955) and Geertsma and De Klerk (1969) developed the so-called KGD model for the propagation in the horizontal direction of a vertical fracture with a rectangular cross-section, assuming a constant fracture height much larger than the fracture length, and a one-dimensional fluid flow within the fracture; and (iii) Abé et al. (1976) and Advani et al. (1987) developed a propagation model for a two-dimensional penny-shaped hydraulic fracture, accounting for two-dimensional fluid flow within it (**Fig.1a**).

To remain mathematically tractable, these analytical models are generally based on simplifying assumptions corresponding to asymptotic regimes that can be relevant in specific conditions. In practice though, they only offer approximate solutions to actual, more complex problems in the field, e.g., heterogeneity of the rock formation or fluid leak-off within the fracture. In fact, hydromechanical coupling and the impact of the boundary conditions (far field stress) will lead to non-linear fracture propagation locally, which must be captured in order to achieve robust and accurate predictions for a specific application.

To address the inherent limitations of analytical models, numerical simulations of fracture propagation in pseudo-3D were introduced in the early 70s (Simonson et al. 1978; Fung et al. 1987), followed by more accurate but costly planar-3D (PL3D) models (Clifton and Abou-Sayed 1981; Vandamme and Curran 1989; Advani et al. 1990; Clifton and Wang 1991; Naceur et al. 1990). Recently, Lecampion and Desroches (2015) presented a PL3D model for the initiation and propagation of a radial fracture based on an implicit time-stepping scheme and involving the Displacement Discontinuity Method (DDM) (Lecampion and Detournay 2007).

Notably, this model captures the initiation and early-time propagation of the fracture, when nonlinearity dominates. Alternatively, the time and scale integration of multiple tip asymptotic solutions to predict hydraulic fracture propagation leads to a good agreement with experimental data for homogeneous and brittle materials such as Polymethyl Methacrylate (PMMA), or synthetic cement/sand samples (Garagash and Detournay 2000; Savitski and Detournay 2002; Lecampion et al. 2017; Lecampion and Detournay 2007; Bungler and Detournay 2007). However, this approach requires to iteratively track the front of the propagating fracture and update the system of equations, which is computationally costly in practice. In addition, the application of the DDM is restricted to homogenous and linear elastic solids (Lecampion and Desroches 2015). For heterogeneous rocks with non-local deformation around the fracture tip (process zone) a discrepancy exists between model predictions and experimental observations, typically in terms of wellbore pressure and fracture width (Lecampion et al. 2017). Note also that computational costs are aggravated when modelling heterogeneous or anisotropic reservoirs.

Linear hydraulic fracture mechanics (LHFM) incorporates linear elastic fracture mechanics (LEFM) and Poiseuille's flow law. This approach is widely used to model the growth of a hydraulic fracture in homogeneous and brittle materials such as PMMA or glass (Bunger and Detournay 2008; Liu 2021). However, the nonlinearity induced by the deformation and energy dissipation taking place in the cohesive (process) zone, and by fluid flow near the tip region within quasi-brittle materials (e.g., sedimentary rock) are often neglected (Liu 2021). Earlier studies show that the LHFM approach is suitable for low ratio of confining to cohesive stress (σ_o/σ_c). Significant deviations from LHFM predictions are observed in laboratory or field applications when the dimensionless ratio σ_o/σ_c becomes large (Adachi et al. 2007; Garagash 2019). This may explain the discrepancy observed between numerical simulation results and experimental observations for heterogeneous rocks subjected to realistic triaxial stress fields (De Pater et al. 1994b; van Dam et al. 2000; Lecampion et al. 2017). For example, Poiseuille's cubic flow law is well accepted for modelling the laminar flow of highly viscous fluids such as magma within fractures, where the process zone is embedded in the fluid lag zone (**Fig.1b**). However, for a low-viscous fracturing fluid (e.g., slick water or gel), the lag zone is usually embedded in the process zone (**Fig.1c**), where the cubic flow law is no longer valid (Garagash 2019). Therefore, for quasi-brittle materials, the determination of the fluid lag and cohesive zone adjacent to the crack tip are necessary for validating the use of Poiseuille's cubic flow law in modelling hydraulic fracturing.

Simultaneous measurement of the borehole pressure (BHP), fracture radius (R), and width/aperture (w) of a hydraulic fracture under true triaxial stress condition (TTSC) are scarce in the literature (De Pater et al. (1994b); Lhomme (2005)). In the laboratory, the width of hydraulic fracture can be estimated by measuring the bulk deformation of the rock sample with Linear Variable Differential Transformers (LVDT) attached to its faces, or internal LVDTs located within the wellbore. However, tracking the evolution of the fracture's radius is technically more challenging. Such radius estimations were traditionally performed on samples of transparent material with a high-speed camera (Bunger 2005), or using active and/or passive ultrasonic monitoring (De Pater et al. 1994b; Lhomme 2005; Nabipour 2013). To overcome the aforementioned mathematical, numerical, or experimental challenges for tracking the extent of a hydraulic fracture, it is essential to develop a robust model using the less and most reliable input data, for application to the widest range of underground stimulation projects.

Here, we develop a new analytical model for the temporal evolution of the fracture radius R_d for a radial hydraulic fracture (**Fig.1a**). For this R_d model, and based on dimensional analysis, we discuss the possible propagation regimes for various near-tip conditions (i.e., cohesive zone, fluid lag). For comparison, we also quantify the radius based on linear elastic fracture growth model (R_E), and asymptotic solutions (R_v and R_T). The three analytical models are then verified using literature data (i.e., Seven different materials: Cement/Sand, Colton and Felser sandstones, and PMMAs). Finally, the results and recommendations of the R_d model are discussed. **Table 1** compares the characteristics of the existing methods from the literature and the newly R_d model defined in this paper.

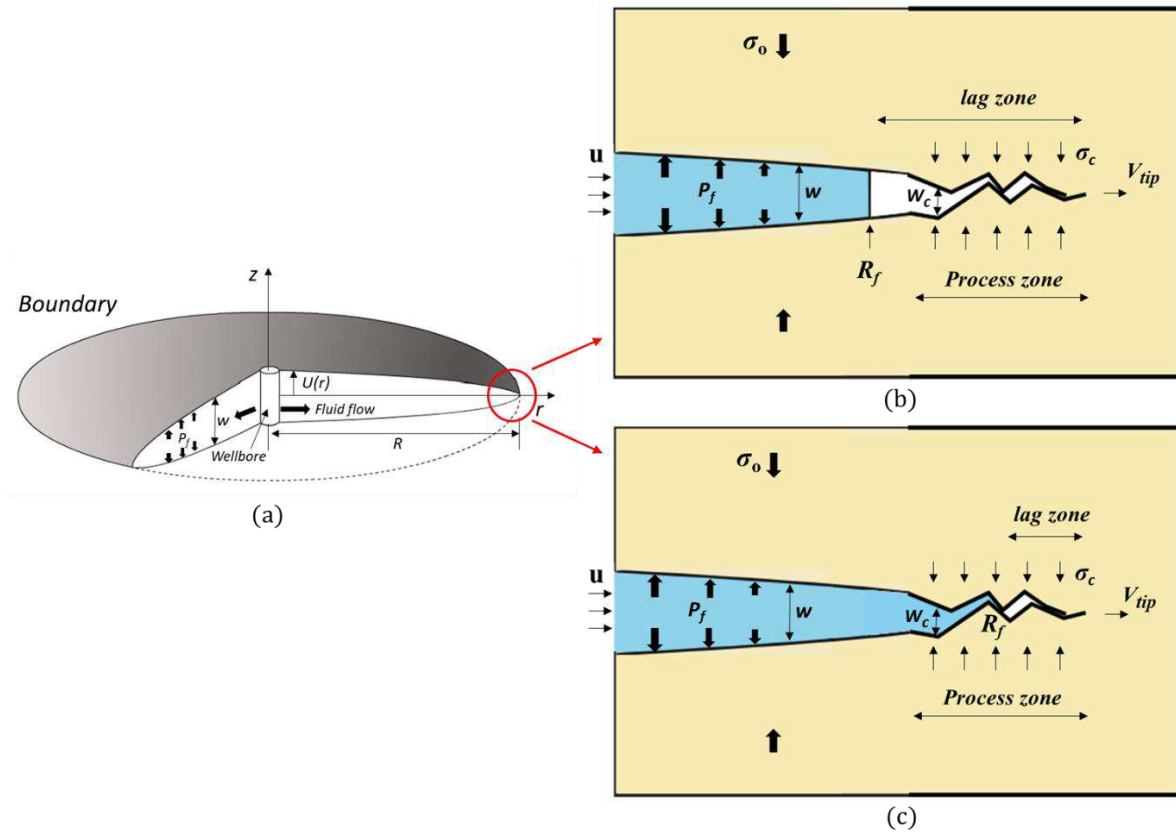


Fig.1 Schematic of penny-shaped hydraulic fracture **a)** 3D geometry of propagation adapted from Savitski and Detournay (2002) and Valkó and Economides (1995), **b)** the near-tip region modelled as Poiseuille flow with significant lag in a semi-infinite crack (image modified from Garagash (2015)) and **c)** the near-tip region modelled as “rough” channel flow with limited lag zone in a semi-infinite crack (image modified from Garagash (2019)).

Table 1. Radius prediction of penny-shaped hydraulic fracture: Comparison between existing methods and our new developed analytical model R_d

	Reference	Assumption	Early-time initiation	Fluid lag	Cohesive zone
Analytical approximation	Abé et al. 1976; Advani et al. 1987	Homogeneous, linear elastic medium			
Asymptotic solutions	Savitski and Detournay 2002; Detournay 2004	Homogeneous, linear elastic medium		✓	
Numerical work	Lecampion and Desroches (2015); Lecampion et al (2017)	Homogeneous isotropic medium	✓	✓	
Experimental measurement	Lhomme (2005); Nabipour (2013)	N/A	✓		
Temporal radius model R_E (analytical)	Sneddon (1946); Valkó and Economides (1995)	linear elastic medium	✓		
Temporal radius model R_d (analytical)	Defined in this paper	Self-similar propagation	✓	✓	✓

2. Fracture propagation models

2.1 Elastic fracture growth model (R_E)

Linear elasticity is widely applied for static equilibrium of solids (Green and Zerna 1992; Valkó and Economides 1995). For the propagation of a penny-shaped fracture (**Fig.1a**), borehole pressure (BHP) is a function of mechanical properties (Young's modulus E and Poisson's ratio ν), fracture dimensions (radius R and width w), and time t , i.e., $\text{BHP} = f(w, R, E, \nu, t)$. The propagation of hydraulic fractures can be described by linear elasticity using the Fourier transform (Sneddon 1995). Solving the initial-boundary value problem for a penny-shaped fracture propagating from a borehole at $r = 0$ entails constructing an auxiliary function $g(\xi)$ (Green and Zerna 1992; Sneddon 1995; Valkó and Economides 1995), i.e.,

$$g(\xi) = \frac{2}{\pi} \int_0^\xi \frac{P(\xi)}{(\xi^2 - r^2)^{\frac{1}{2}}} r dr, \text{ with } 0 < \xi < R, \quad (1)$$

where ξ is a dummy length variable; $g(\xi)$ possesses the dimension of a fluid pressure P ; r is a point on the fracture surface, and R is the radius of the fracture at a given time t . Considering **Eq. (1)**, the normal displacement of any point on the upper part of the fracture disk reads

$$U_z(r) = \frac{2}{E'} \int_r^R \frac{g(\xi)}{(\xi^2 - r^2)^{\frac{1}{2}}} \xi d\xi, \text{ with } 0 \leq r \leq R, \quad (2)$$

where E' is the plane strain modulus.

The fluid pressure within a real hydraulic fracture is not uniform, and more complex fluid pressure distributions can be approximated by a polynomial Taylor expansion in terms of the small variable ξ , i.e.,

$$P(\xi) = P_0 + \frac{P_1}{1!} \xi + \frac{P_2}{2!} \xi^2 + o(r^3) \quad (3)$$

Where P_0 is the initial fluid pressure at the wellbore (zeroth-order), P_1 , and P_2 are the primary and secondary pressure gradients (i.e., $P_1 = \frac{\partial p}{\partial r}$ and $P_2 = \frac{\partial^2 p}{\partial^2 r}$), which are unfortunately difficult to determine in practice.

For sake of simplicity, we assume a uniform fluid pressure within the fracture, $P(\xi) = P_0$, the auxiliary function **Eq. (1)** reduces to

$$g(\xi) = P_0 \xi. \quad (4)$$

Integration of **Eq. (2)** over the radius r yields the fracture's aperture $w = 2 U_z(r)$, i.e.,

$$w(r) = \frac{8}{\pi E'} P_0 \sqrt{R^2 - r^2}, \text{ with } 0 \leq r \leq R. \quad (5)$$

For an elliptical cross-section of the fracture (see **Fig.1a**), the maximum width occurs at the wellbore ($r = 0$), thus **Eq. (5)** reduces to

$$w_{\max}(r = 0) = \frac{8}{\pi E} P_o R. \quad (6)$$

Correspondingly, fracture width is nominally zero at the tip, where $r = R$, i.e.,

$$w_{\min}(r = R) = 0. \quad (7)$$

2.2 Self-similar fracture growth model (R_d)

Considering a possible fluid lag (see **Figs. 1b and 1c**), we introduce the fluid radius R_f , smaller or equal (if no lag) to the fracture radius R , i.e., $R_f < R$. Poiseuille's law is used to describe the flow of a Newtonian fluid driven by fluid pressure within a penny-shaped fracture (Batchelor and Batchelor 2000; Lecampion et al. 2017)

$$q(r, t) = w(r, t) u(r, t) = -\frac{w(r, t)^3}{12 \mu_f} \frac{\partial p_f(r, t)}{\partial r}, \text{ with } 0 < r < R_f < R, \quad (8)$$

where q is the flow rate per unit of fracture perimeter; w is the width/aperture of the fracture; p_f is the fluid pressure within the fracture; $u(t) = dR_f(t)/dt$ is the velocity of the fluid at the fluid front $r = R_f(t)$; and μ_f is the viscosity of the fluid. Note that $R_f = R_f(t)$ and $R = R(t)$ are time-dependent during fracture propagation.

Assuming a self-similar (homothetic) hydraulic fracture growth for **Eq. (8)** (see **Fig.2**), and considering Stefan condition at the interface between the fluid front and the lag at $r = R_f(t)$, leads to (Lecampion et al. 2017)

$$\frac{dR_f(t)}{dt} = -\left. \frac{w^2}{12 \mu_f} \frac{\partial p_f(r, t)}{\partial r} \right|_{r=R_f} \text{ at } r = R_f, \quad (9)$$

where the change in fluid pressure with radius at $r = R_f$, i.e., $\left. \partial p_f(r, t) / \partial r \right|_{r=R_f}$, is difficult to evaluate in practice, whether in the laboratory or in the field. Eq. (9) can be rewritten as (see derivation in **Appendix A.1**)

$$\frac{dR_f(t)}{dt} = \sqrt{\left. \frac{w^2}{12 \mu_f} \frac{\partial p_f(r, t)}{\partial t} \right|_{r=R_f}} \text{ at } r = R_f, \quad (10)$$

which now involves the change in fluid pressure with time at the fluid front $r = R_f$, i.e., $\left. \partial p_f(r, t) / \partial t \right|_{r=R_f}$. Although the fluid pressure variations within the borehole (i.e., at the fracture inlet) are known, the fluid pressure variations at the moving fluid front $r = R_f$ during fracture propagation is difficult to evaluate, whether in the laboratory or in the field.

Therefore, we further assume that for a given time increment the pressure-time variations at the fluid front and at the fracture inlet (borehole) are proportional (see justification in **Appendix A.2**), i.e.,

$$\left. \frac{\partial p_f(r,t)}{\partial t} \right|_{r=R_f} \cong -\lambda_p(t) \left. \frac{\partial p_f(r,t)}{\partial t} \right|_{r=0} = -\lambda_p(t) \frac{dp_o(t)}{dt}, \quad (11)$$

where $dp_o(t)/dt$ is the borehole pressure-time variations often recorded in laboratory experiments or field stimulation operations. This assumption of proportionality at each time increment during propagation ultimately implies that the proportionality coefficient can in principle be time-dependent, i.e., different for consecutive time increments $\lambda_p = \lambda_p(t)$. However, based on laboratory fracturing data reported in the literature (see **Appendix A.3** for details), the proportionality coefficient $\lambda_p(t)$ is found to be relatively constant during propagation for a given fracturing experiment. This empirical observation allows us to simplify **Eq. (11)** to

$$\left. \frac{\partial p_f(r,t)}{\partial t} \right|_{r=R_f} \cong -\lambda_p \frac{dp_o(t)}{dt}. \quad (12)$$

Combining **Eqs.(10) and (12)** yields

$$\frac{dR_f(t)}{dt} \cong \sqrt{-\lambda_p \frac{w^2}{12 \mu_f} \frac{dp_o(t)}{dt}}. \quad (13)$$

Note that even when a fluid lag exists, it is small compared to R , and gets smaller with time during propagation (Savitski and Detournay 2002). Therefore, we thus further assume that $R_f \approx R$. Therefore, **Eq. (13)** can be rewritten as

$$\frac{dR(t)}{dt} \cong \sqrt{-\lambda_p \frac{w^2}{12 \mu_f} \frac{dp_o(t)}{dt}}. \quad (14)$$

Eq.(14) can be discretised and applied to laboratory measurements of wellbore pressure $p_o(t)$ during fracturing (see **Fig.3**), i.e.,

$$\frac{\Delta R}{\Delta t} \cong \sqrt{-\lambda_p \frac{w^2}{12 \mu_f} \frac{\Delta p_o}{\Delta t}} \quad (15)$$

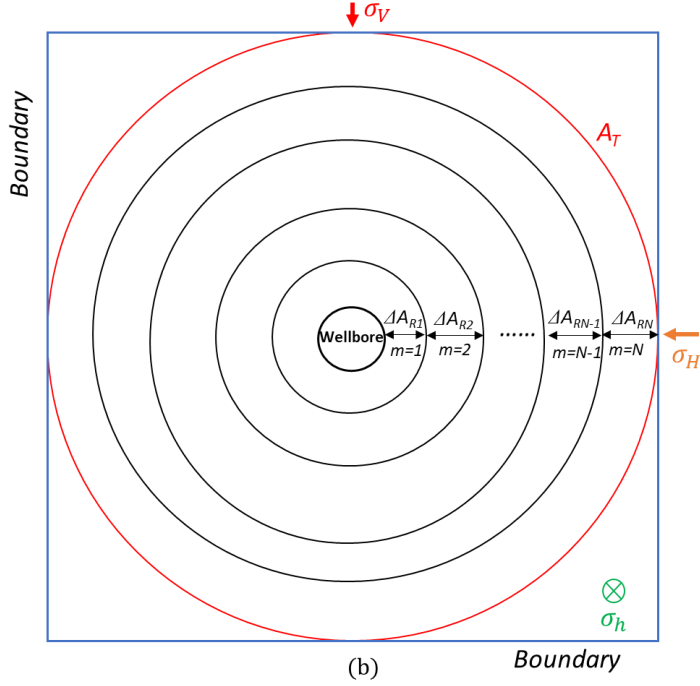


Fig.2 2D schematic of the self-similar evolution of the radial fracture, outlining the temporal fracture surface area A_d .

Experimental results reported in the literature suggest that laboratory-scale transverse or longitudinal hydraulic fractures in low permeability rocks are approximately penny-shaped (Bunger 2005; Lhomme 2005; Rodriguez and Stanchits 2017; Sarmadivaleh 2012). In this context, the total time-cumulated volume of incompressible fluid injected into the fracture propagating from the wellbore by the end of propagation, i.e., when $R = R_T$, is $V_T = 2\pi \int_0^{R_T} w r dr = \pi w R_T^2$. Similarly, the time-cumulated volume at any time t , when the fracture reaches a radius $R(t) < R_T$ during propagation, is related to the average (constant) injection flow rate Q_{in} by

$$V(t) = 2\pi \int_0^R w R dR = \pi w R^2 = w A_R = Q_{in} t, \quad (16)$$

where $A_R = \pi R^2$ is the fracture's surface area at time t . For a self-similar (homothetic) propagation of the penny-shaped fracture, for a small enough incremental increase in fracture surface area $(\Delta A_R)_m$ per time increment Δt_m , and noting that $\frac{dA_R}{dt} = 2\pi R \frac{dR}{dt}$, **Eq.(15)** becomes

$$\frac{(\Delta A_R)_m}{\Delta t_m} \cong 2\pi R_m \sqrt{\lambda_p} \sqrt{-\frac{w^2}{12\mu_f} \left(\frac{\Delta p_o}{\Delta t}\right)_m}, \quad \text{with } 1 \leq m \leq N, \quad (17)$$

where $2\pi R_m$ is the circumference of the self-similarly moving boundary of the growing penny-shaped fracture (**Fig.2**), and N is the total number of time increments. **Eq. (17)** indicates that

$(\Delta A_R)_m$ is proportional to $\sqrt{-\frac{w_m^2}{12\mu_f} \left(\frac{\Delta p_o}{\Delta t}\right)_m}$, where a new proportionality coefficient $\lambda_m(t) = 2\pi R_m \Delta t_m \sqrt{\lambda_p}$ and an intercept B_m are introduced so that

$$(\Delta A_R)_m \cong \lambda_m(t) \sqrt{-\frac{w_m^2}{12\mu_f} \left(\frac{\Delta p_o}{\Delta t}\right)_m} + B_m, \text{ with } 1 \leq m \leq N. \quad (18)$$

Let A_T be the total (maximum) fractured area, obtained when the fracture reaches the boundaries of the rock sample, where $R = R_T$. The time-dependent surface ratio $(\Delta A_R)_m/A_T$ reads

$$\frac{(\Delta A_R)_m}{A_T} \cong \frac{\lambda_m(t) \sqrt{-\frac{w_m^2}{12\mu_f} \left(\frac{\Delta p_o}{\Delta t}\right)_m} + B_m}{\sum_{i=1}^N \left(\lambda_i(t) \sqrt{-\frac{w_i^2}{12\mu_f} \left(\frac{\Delta p_o}{\Delta t}\right)_i} + B_i \right)}, \text{ with } 1 \leq i \leq N \text{ and } 1 \leq m \leq N \quad (19)$$

where the indices i and m reflect the time steps between the nucleation ($i = m = 1$) and the end of propagation ($i = m = N$) of the hydraulic fracture, i.e., when it reaches the boundaries of the rock sample. Fitting **Eq.(18)** to the fracture growth data published in the literature, we observe that $\lambda_m(t) \cong \lambda$ is approximately constant for a given propagation experiment, and that B_m is negligibly small, i.e., $B_m \ll (\Delta A_r)_m$ (see details in **Section 3.3**). Therefore, **Eq.(19)** can be approximated by

$$(\Delta A_R)_m \cong \frac{A_T \sqrt{-\frac{w_m^2}{12\mu_f} \left(\frac{\Delta p_o}{\Delta t}\right)_m}}{\sum_{i=1}^N \sqrt{-\frac{w_i^2}{12\mu_f} \left(\frac{\Delta p_o}{\Delta t}\right)_i}}, \text{ with } 1 \leq i \leq N \text{ and } 1 \leq m \leq N \quad (20)$$

Finally, the cumulative increase in fracture area with time, A_d between fracture nucleation, $m = 1$ and a later time step, $m = n$ (where $n \leq N$) reads (see **Fig.2**)

$$A_d \cong \sum_{m=1}^n (\Delta A_R)_m = A_T \frac{\sum_{m=1}^n \left(\sqrt{-\frac{w_m^2}{12\mu_f} \left(\frac{\Delta p_o}{\Delta t}\right)_m} \right)}{\sum_{i=1}^N \left(\sqrt{-\frac{w_i^2}{12\mu_f} \left(\frac{\Delta p_o}{\Delta t}\right)_i} \right)}, \text{ with } 1 \leq i \leq N \text{ and } 1 \leq m \leq n \leq N \quad (21)$$

Furthermore, **Eq.(14)** indicates that w is proportional to $\frac{dR}{dt}$ where the Poiseuille's law (**Eq.8**) is still valid when the energy dissipation is dominated by fluid flow within the fracture (Garagash D and Detournay E 2000; Peck et al. 2018; Garagash 2019). In contrast, when energy dissipation is dominated by cohesive-zone effects near the tip region (Lhomme 2005; Sarris and Papanastasiou 2011; Garagash 2019; Liu and Lecampion 2021), (i) the fracture opens

smoothly, i.e., w becomes proportional to $\left(\frac{dR}{dt}\right)^{\frac{3}{2}}$, ($w \propto \left(\frac{dR}{dt}\right)^{\frac{3}{2}}$) (Garagash and Detournay (2000); Garagash (2019)), and (ii) the coefficient of proportionality remains the same as for the Poiseuille's fluid condition, i.e., $\sqrt{-\frac{1}{12\mu_f} \frac{dp_o}{dt}}$. In this case, **Eq. (15)** is replaced by

$$\frac{\Delta R}{\Delta t} \cong \sqrt[3]{-\lambda_p \frac{w^2}{12\mu_f} \frac{\Delta p_o}{\Delta t}}, \quad (22)$$

and **Eq.(21)** is replaced by

$$A_d \cong A_T \frac{\sum_{m=1}^n \left(\sqrt[3]{-\frac{w_m^2}{12\mu_f} \left(\frac{\Delta p_o}{\Delta t}\right)_m} \right)}{\sum_{i=1}^N \left(\sqrt[3]{-\frac{w_i^2}{12\mu_f} \left(\frac{\Delta p_o}{\Delta t}\right)_i} \right)}, \quad \text{with } 1 \leq i \leq N \text{ and } 1 \leq m \leq n \leq N \quad (23)$$

For all propagation regimes the equivalent radius of the fracture R_d is defined as

$$R_d = \sqrt{\frac{A_d}{\pi}}. \quad (24)$$

2.3 Fracture propagation regimes and asymptotic solutions

A dimensionless group, i.e., time scale (t_{om} , t_{mk}), dimensionless toughness (k), and the time scale ratios (χ , Ψ) have been introduced to analyse fracture propagation regimes (Savitski and Detournay 2002; Detournay 2004; Garagash 2006; Bungler and Detournay 2007; Lecampion et al. 2017; Lhomme 2005; Dontsov 2016). A set of three scaled material parameters were defined by dimensional analysis

$$\begin{aligned} K' &= \left(\frac{32}{\pi}\right)^{\frac{1}{2}} K_{IC}, \\ E' &= \frac{E}{1-\nu^2} K_{IC}, \\ \mu' &= 12\mu, \end{aligned} \quad (25)$$

where K_{IC} is the fracture toughness, E is Young's Modulus, ν is Poisson's ratio, and μ is the viscosity of the fluid. For a constant fluid injection rate Q_{in} , a time scale t_{mk} is defined as the time required for fracture propagation to evolve from a viscosity-dominated regime at early times to a toughness-dominated one at larger times, i.e.,

$$t_{mk} = \left(\frac{\mu'^5 Q_{in}^3 E'^{13}}{K'^{18}} \right)^{\frac{1}{2}}, \quad (26)$$

and a dimensionless toughness k is introduced for discriminating the two propagation regimes, i.e.,

$$k = K' \left(\frac{t^2}{\mu'^5 Q_{in}^3 E'^{13}} \right)^{\frac{1}{18}}. \quad (27)$$

When $k \leq 1$, the propagation regime is viscosity dominated; while for $k \geq 3.5$, the regime is said to be toughness dominated (Savitski and Detournay 2002).

The analytical asymptotic solutions of radius for a radial hydraulic fracture reads for viscosity dominated regime (Savitski and Detournay 2002; Detournay 2004; Chen et al 2017):

$$R_V = R(t) = 0.696 \left(\frac{E'}{\mu' Q_{in}} \right)^{\frac{1}{9}} (Q_{in} t)^{4/9} \quad (28)$$

And for toughness dominated regime:

$$R_T = R(t) = \left(\frac{3}{\sqrt{2}\pi} \right)^{\frac{2}{5}} \left(\frac{E'}{K'} \right)^{\frac{2}{5}} (Q_{in} t)^{\frac{2}{5}} \quad (29)$$

Eq.(28) defining R_V , or **Eq.(29)** defining R_T are used for fracture radius predictions and comparison to the two models introduced earlier (R_E and R_d) and to experimental data.

A time scale ratio χ is also introduced to capture the transition from the early-time fracture initiation driven by the compressibility of the injection system, to the large-time steady propagation at a constant injection rate Q_{in} (Lecampion et al. 2017), i.e.,

$$\chi = \frac{E'^4 Q_{in}^{3/2} \mu'^{3/2}}{K'^6 U^{1/2}}, \quad (30)$$

where U is the volumetric compliance of the injection system, i.e., combined compressibility of the fluid and the pumping system. A time scale t_{om} is also introduced in relation to the coalescence of the fluid front and fracture tip, when the fluid lag goes to zero, i.e.,

$$t_{om} = \frac{E'^2 \mu'}{\sigma_o^3}, \quad (31)$$

where σ_o is the compressive stress orthogonal to the fracture surface. A second time scale ratio Ψ is introduced for the transition from the toughness-dominated regime driven by fluid lag, to the large-time propagation regime where fluid front and fracture tip coincide (Lecampion et al. 2017)

$$\Psi = \frac{t_{mk}}{t_{om}} = \left(\frac{E'^{3/2} Q_{in}^{1/2} \mu'^{1/2} \sigma_o}{K'^3} \right)^3. \quad (32)$$

Garagash (2015), Garagash (2019), and Liu and Lecampion (2021) showed that (see summary in **Table 2**)

- (i) If $k < 1$ and $\Psi \gg 1$, the fracture propagates in a viscosity-dominated regime with significant fluid lag (**Fig.1b**); in this situation Poiseuille's flow law is valid, and **Eqs. (21) and (24)** can be used to estimate A_d and R_d , respectively;

- (ii) If $1 \leq k \leq 3.5$ and $\Psi \ll 1$, the fracturing fluid invades the process zone (**Fig.1c**), resulting in local turbulent flow and slight deviation from Poiseuille's flow law (Liu and Lecampion 2021); in this situation **Eqs. (23) and (24)** can be used to estimate A_d and R_d , respectively;
- (iii) If $1 \leq k \leq 3.5$ and $\Psi \gg 1$, the ratio of confining stress to cohesive stress, σ_o/σ_c , becomes critical. A large σ_o/σ_c ratio accelerates the penetration of the fluid into the cohesive zone, and is modelled as inversely proportional to the size of the fluid lag zone (Garagash 2019; Liu and Lecampion 2021). For instance, the numerical results reported by Liu and Lecampion (2021) suggest that for a dimensionless toughness $k = 2$, the fluid fraction ζ ranges from 0.85 to 0.98 when σ_o/σ_c ranges from 1 to 10. In this situation, the ratio between the size of the fluid lag and that of the cohesive zone is relatively small. Therefore, we argue that this situation is similar to case (ii), and **Eqs. (23) and (24)** can be used to estimate A_d and R_d , respectively;
- (iv) If $k > 3.5$, a strongly toughness-dominated propagation regime, the fluid lag-to-cohesive zone size ratio is also small (Bunger et al. 2013; Liu and Lecampion 2021). In this situation, a relatively large amount of fluid invades the anticipated large cohesive zone, especially for a low σ_o/σ_c ratio (Liu and Lecampion 2021). We again argue that in this situation **Eqs. (23) and (24)** can be used to estimate A_d and R_d , respectively;
- (v) The aforementioned conditions (i)-(iv) only apply to conventional rocks for which the peak tensile stress (cohesive strength) lies in the range 2MPa to 12MPa (Rybacki et al. 2015). In contrast, for brittle materials like PMMA or glass, the tensile strength lies in the range 60 to 70MPa (Zhou et al. 2018), resulting in a very limited extent of the cohesive zone (Garagash 2019). Therefore, for PMMA or glass, **Eq. (21)** is used instead of **Eq. (23)** for quantifying A_d .

Table.2 Fracture propagation regimes

Condition	Propagation regime	Fluid Lag	Poiseuille law	Equation for A_d model
$k < 1, \Psi \gg 1$	Viscosity dominated	Significant	Valid	Eq.(21)
$1 \leq k \leq 3.5, \Psi \ll 1$	Transitional	Minor	Invalid	Eq.(23)
$1 \leq k \leq 3.5, \Psi \gg 1$	Transitional	Minor	Invalid	Eq.(23)
$\sigma_o/\sigma_c > 1$				
$k > 3.5$	Toughness dominated	Minor	Invalid	Eq.(23)
PMMA or Glass	Toughness dominated	Significant	Valid	Eq.(21)

3. Validation of the self-similar fracture propagation model (R_d)

3.1 Experimental input data

We use the literature data recorded during hydraulic fracturing experiments conducted on synthetic rock analogues subjected to true triaxial stress conditions, i.e., cement/sand blocks from De Pater et al. (1994a), and tight sandstone blocks (Colton and Felser) from Lhomme (2005). These data sets include simultaneous monitoring of wellbore pressure, fracture radius, and strains induced by hydraulic fracturing. Additionally, data from two PMMA blocks subjected to biaxial stresses are also considered as a brittle/homogeneous end-member (Bunger et al. 2013).

As shown in **Table 3**, the propagation of hydraulic fractures can be classified as stable or unstable according to the experimental conditions (De Pater et al. 1994a; Lhomme 2005; Bunger et al. 2013). The permeability of Colton 08 and 09 ranges from 0.15 to 0.3 mD, while it is one order of magnitude lower for Cov12c, i.e., ~ 0.02 mD; fluid leak-off through the fracture walls is therefore ignored for the typical duration of a laboratory hydraulic fracturing experiment. However, the permeability of the Felser sandstone samples is in the range 2 to 5 mD, which implies that pressurized fracturing fluid can leak into the pore space of the sample during the experiment (Lhomme 2005). Based on their petrophysical properties, the seven rock samples are classified into four groups: (i) stable fracture propagation without leak-off, i.e., Cov12c and Colton 08; (ii) stable fracture propagation with leak-off, i.e., Felser 02; (iii) unstable fracture propagation without leak-off, i.e., Colton 09, ab5, c11m1; and (iv) unstable fracture propagation with leak-off, i.e., Felser 03.

In the case of a stable fracture propagation (**Fig.3a**), the early-time fracture nucleation process dissipates a significant amount of energy, resulting in the fracture propagating at a wellbore pressure much lower than the maximum wellbore breakdown pressure(See Appendix B for correction of the depressurization rate prior to breakdown), and the rate of wellbore pressure drop to zero is relatively small. The fracture radius and width gradually increase to reach a plateau. In the case of an unstable fracture propagation (**Fig.3b**), fracture initiation and borehole breakdown always coincide. In this situation, the fracture radius and width increase virtually instantaneously, and the wellbore pressure drops approximately ten-times faster than in the stable case.

Table.3 Materials parameters and experimental conditions from literature (Bunger et al. 2013; De Pater et al. 1994a; Lhomme 2005)

Sample Type	Young's Modulus E (GPa)	Poisson's Ratio ν (-)	Permeability K (mD)	Confining Stress σ_0 (MPa)	Cohesive strength σ_c (MPa)	Propagation Condition	Leak-off
-------------	-------------------------	---------------------------	---------------------	-----------------------------------	------------------------------------	-----------------------	----------

Cov12c	Cement/Sand	24	0.25	0.02	9.7	3.5	Stable	No
Colton 08	Very Tight Sandstone	20	0.17	0.15-0.3	10	3	Stable	No
Colton 09	Very Tight Sandstone	14	0.17	0.15-0.3	10	3	Unstable	No
Felser 02	Tight Sandstone	15	0.2	2-5	10	2	Stable	Yes
Felser 03	Tight Sandstone	15	0.2	2-5	10	2	Unstable	Yes
ab5	PMMA	3.3	0.4	0	0	44	Unstable	No
c11m1	PMMA	3.3	0.4	0	0	44	Unstable	No

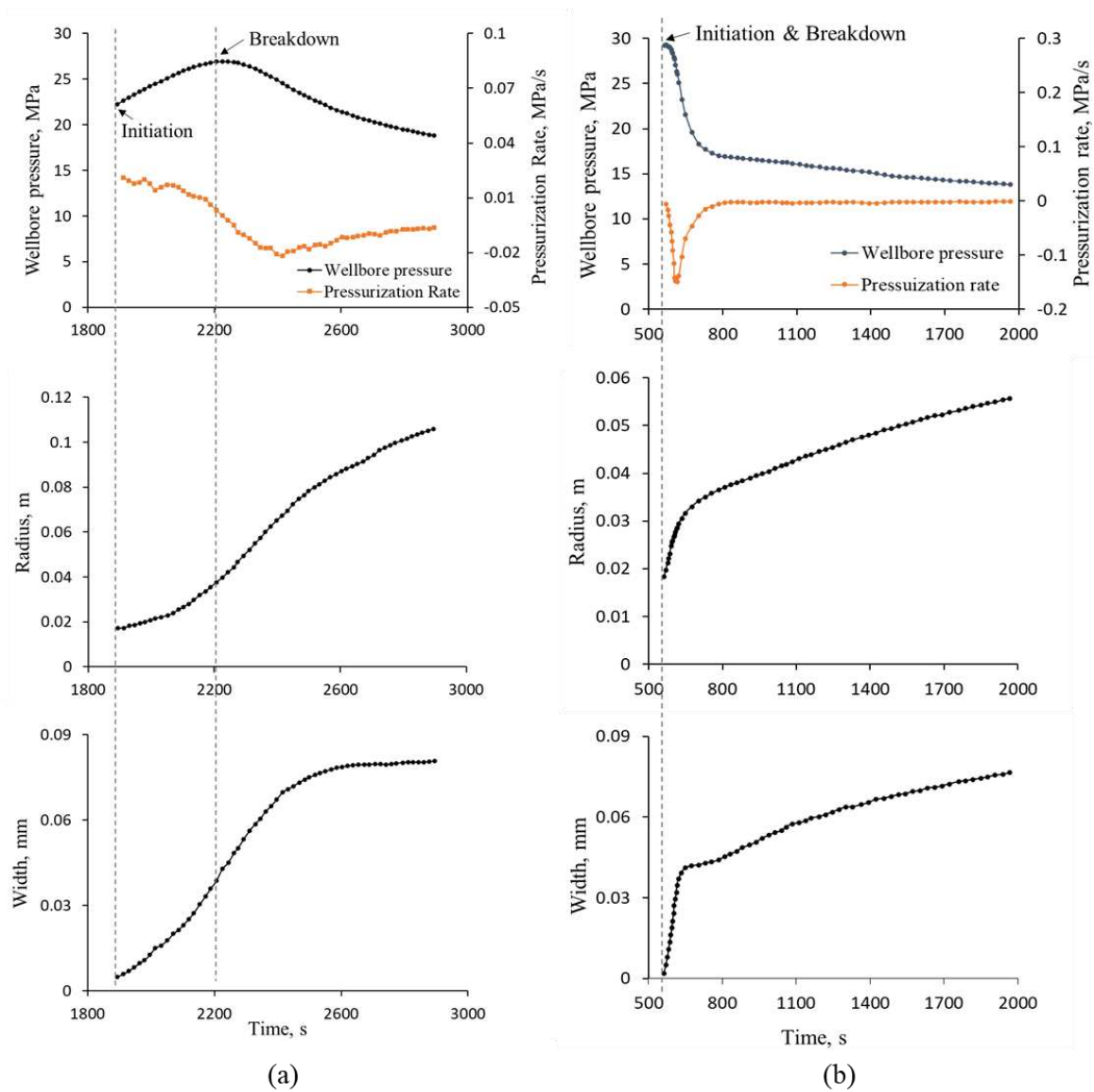


Fig.3 Experimental results of wellbore pressure, fracture radius, and width (De Pater et al. 1994b; Lhomme 2005): a) Cov12c, stable propagation and b) Felser 03, unstable propagation

3.2 Dimensionless parameters

The values of the time scales t_{mk} and t_{om} , the dimensionless toughness (k), the time scale ratios χ and Ψ , and the ratio of confining stress to cohesive strength (σ_o/σ_c) for each sample are reported in **Table 4**. These dimensionless parameters are used here to predict the characteristics of fracture propagation in terms of stability.

3.2.1 Stable fracture propagation

- **Sample Cov12c:** The dimensionless toughness $k = 0.43$ indicates that the propagation regime is strongly viscosity-dominated in the far-field conditions (i.e., $t_{mk} \gg t_{EXP}$); and $\Psi \gg 1$ indicates that there is strong fluid lag during propagation. Therefore, **Eqs. (21) and (24)** based on Poiseuille's flow law are used for the prediction of the fracture's radius R_d .
- **Sample Colton 08:** The $k = 1.20$ indicates a transition from a viscosity- to a toughness-dominated propagation regime; and $\Psi \ll 1$ indicates that fluid lag is negligible during the propagation. Therefore, **Eqs. (23) and (24)** based on the modified Poiseuille's flow law are used to estimate R_d .
- **Sample Felser 02:** The $k = 1.86$ also indicates a transition from a viscosity- to a toughness-dominated propagation regime; and $\Psi = 215$ indicates that fluid lag can occur; however, the relatively large ratio $\sigma_o/\sigma_c = 5$ suggests that the fraction of fluid lag to cohesive zone is relatively small (Liu and Lecampion 2021). Therefore, **Eqs. (23) and (24)** are again used to estimate R_d .

3.2.2 Unstable fracture propagation

- **Sample Felser 03:** The $k = 3.4$ indicates that the fracture propagation regime is essentially toughness dominated; and $\Psi = 21.5$ implies that fluid lag can occur, although this effect is partly compensated by the relatively large stress ratio $\sigma_o/\sigma_c = 5$, which tends to accelerate fluid flow into the process zone, and reduce the fluid lag-to-cohesive zone ratio. Therefore, **Eqs. (23) and (24) are used to estimate R_d .**
- **Sample Colton 09:** The $k = 3.0$ indicates that the fracture propagation regime is essentially toughness dominated; and $\Psi = 3.5$ and $\sigma_o/\sigma_c = 3.3$ suggest that fluid lag is relatively small during propagation. Therefore, **Eqs. (23) and (24)** are used to estimate R_d .
- **Samples ab5 and c11m1 (PMMA):** The $k = 3.5$ for sample ab5, and $k = 5.3$ for sample c11m1 indicate that the fracture propagation regime is essentially toughness dominated (i.e., $t_{EXP} \gg t_{mk}$). These experiments were conducted in the laboratory under the

condition $\sigma_o/\sigma_c = 0$ to allow for high-resolution monitoring of the propagation with a high-speed camera through the transparent PMMA samples. In this situation, fluid lag was not observed during propagation (Bunger 2005; Bunger et al. 2013). Numerical simulations also suggest a very limited fluid lag (Liu and Lecampion 2021). It is worth noting that the tensile strength (peak cohesive strength) of PMMA is larger than 60MPa (Zhou et al. 2018), which is orders of magnitude larger than for rocks, resulting in a very limited extent of the cohesive zone in PMMA (Bunger and Detournay 2008; Garagash 2019). Therefore, fluid flow is expected to follow Poiseuille’s law, and **Eqs. (21) and (24)** are used to estimate R_d .

Table.4 Key parameters governing the propagation regime of laboratory hydraulic fracturing experiments reported in the literature: Experimental propagation duration (t_{EXP}); compressibility of the injection system (U); dimensionless wellbore radius Λ and notch η ; time scale of the transition from early-time compressibility-dominated regime to large-time constant flow rate regime $t_o^{\wedge}o$ and $t_k^{\wedge}k$; time scale of the transition from viscosity- to toughness-dominated regime t_{mk} ; time scale of the collapse of the fluid lag t_{om} ; dimensionless toughness k ; time scale ratios χ , Ψ by constant injection rate Q_{in} , and ratio of confining stress to cohesive strength (σ_o/σ_c)

	t_{EXP} (s)	U (m ³ /MPa)	Λ	η	$t_o^{\wedge}o$ (s)	$t_k^{\wedge}k$ (s)	t_{mk} (s)	t_{om} (s)	k	χ $= \frac{t_{mk}}{t_m^{\wedge}k^{\wedge}}$	Ψ $= \frac{t_{mk}}{t_{om}}$	σ_o / σ_c
COV12c	1002	1.5e-07	0.064	0.005	620	250	2.23e+06	1181	0.43	235	1886	2.8
Colton 08	2029	2.4e-07	0.134	0.02	1853	2184	421	2545	1.2	0.37	0.17	3.3
Colton 09	10.6	3.2e-07	0.123	0.02	57	65	18	5	3.0	0.45	3.51	3.3
Felser 02	2466	4.0e-07	0.125	0.02	1365	746	3.15e+05	1465	1.86	38	215	5
Felser 03	1404	4.1e-07	0.124	0.02	134	110	787	37	3.4	3.3	21.5	5
ab5	4.3	N/A	N/A	N/A	N/A	N/A	2.1	0	3.5	N/A	0	0
c11m1	9.2	N/A	N/A	N/A	N/A	N/A	0.1	0	5.3	N/A	0	0

3.3 Validation of the fracturing area model (A_d)

Here we validate the model of fracture area A_d using published data detailed in Section 3.1 and 3.2. Four typical cases are presented in this section:

- (i) Stable propagation for a strong viscosity dominated regime ($k=0.43$) in a tight cement-sand sample, i.e., Cov12c
- (ii) Stable propagation for a transitional propagation regime ($k=1.2$) in a very tight sandstone, i.e., Colton 08
- (iii) Unstable propagation for a toughness dominated regime ($k=3.0$) in a very tight sandstone, i.e., Colton 09
- (iv) Unstable propagation for a strong toughness dominated regime ($k=5.3$) in a very hard material (PMMA), i.e., C11m1.

Note that the results for the other PMMA sample ab5 are similar. For sake of completeness, they are reported in **Appendix C.1**. For the Felser 02 and 03 samples where the propagation of hydraulic fracture is affected by the leak-off effect (Lhomme 2005), which is not being fully considered in our A_d model, the validation is additionally reported in **Appendix.C.1and C.3**.

3.3.1 Stable fracture propagation (no leak-off)

Cov12c:

The evolution of the fracture area with time $A_d(t)$ in the cement-sand sample measured by De Pater et al (1994) and predicted with the new A_d model are displayed in **Fig.4**. **Fig.4a** shows that the incremental fracture area per time step $(\Delta A_R)_m$ correlates well with the product $PD_1 = \sqrt{-\frac{w_m^2}{12\mu_f} \left(\frac{\Delta p_o}{\Delta t}\right)_m}$. The resulting linear correlation (robust fitting) shown in **Fig.4b** validates a posteriori the linearity assumption stated in Section 2.2, i.e.,

$$(\Delta A_R)_m = 3.06 \times 10^3 \times \sqrt{-\frac{w_m^2}{12\mu_f} \left(\frac{\Delta p_o}{\Delta t}\right)_m} - 5.55 \times 10^{-7}, \text{ with } R^2 = 0.96 \quad (33)$$

where the value of the y-axis intercept $B = -5.55 \times 10^{-7} \ll (\Delta A_R)_m$. Therefore, **Eq.(20)** can behave closely to **Eq.(19)**. Considering this correlation, the time evolution of the dimensionless parameter of relative change in fracture area $(\Delta A_R)_m/A_T$ and the fraction

$$\frac{\sqrt{-\frac{w_m^2}{12\mu_f} \left(\frac{\Delta p_a}{\Delta t}\right)_m}}{\sum_{i=1}^N \sqrt{-\frac{w_i^2}{12\mu_f} \left(\frac{\Delta p_a}{\Delta t}\right)_i}} \quad \text{are calculated and shown in **Fig.4c**, indicating a$$

reasonably robust fit, despite some measurement-induced fluctuations in $(\Delta A_R)_m/A_T$. Finally, **Fig.4d** compares the predicted evolution of the fracturing area A_d (red triangles) and the experimental data (black dots).

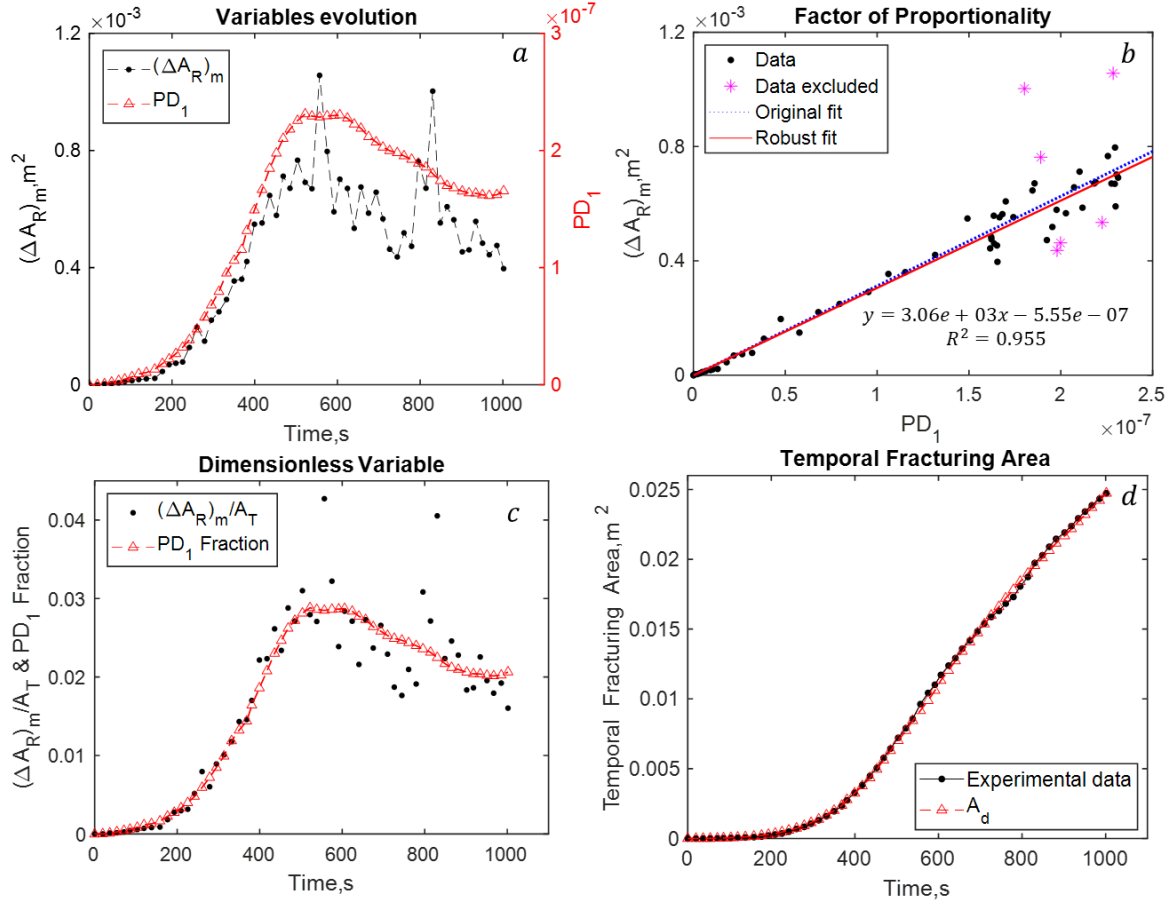


Fig.4 Evolution of the fracture area for the cement/sand sample during stable propagation; Comparison between direct laboratory measurements and predictions of the new model presented here.

Colton 08:

The evolution of the fracture area with time in the Colton 08 sample experimentally measured by Lhomme (2005) and analytically predicted by our A_d model is presented in **Fig.5**. The aforementioned dimensionless parameters suggest that cohesive zone effects are significant in the Colton sandstone (Garagash 2019; Lhomme 2005), which is accounted for in **Eqs.22 and 23** for the Colton 08 sample. Similar to Cov12c, we obtain a reasonably good linear correlation (**Fig.5b**):

$$(\Delta A_R)_m = 15.59 \sqrt[3]{-\frac{w_m^2}{12\mu_f} \left(\frac{\Delta p_o}{\Delta t}\right)_m} - 8.24 \times 10^{-6}, \text{ with } R^2 = 0.9 \quad (34)$$

A good fit is also observed between our analytical prediction and the experimental measurement data in terms of fracturing area growth with time (see **Figs.5c and 5d**).

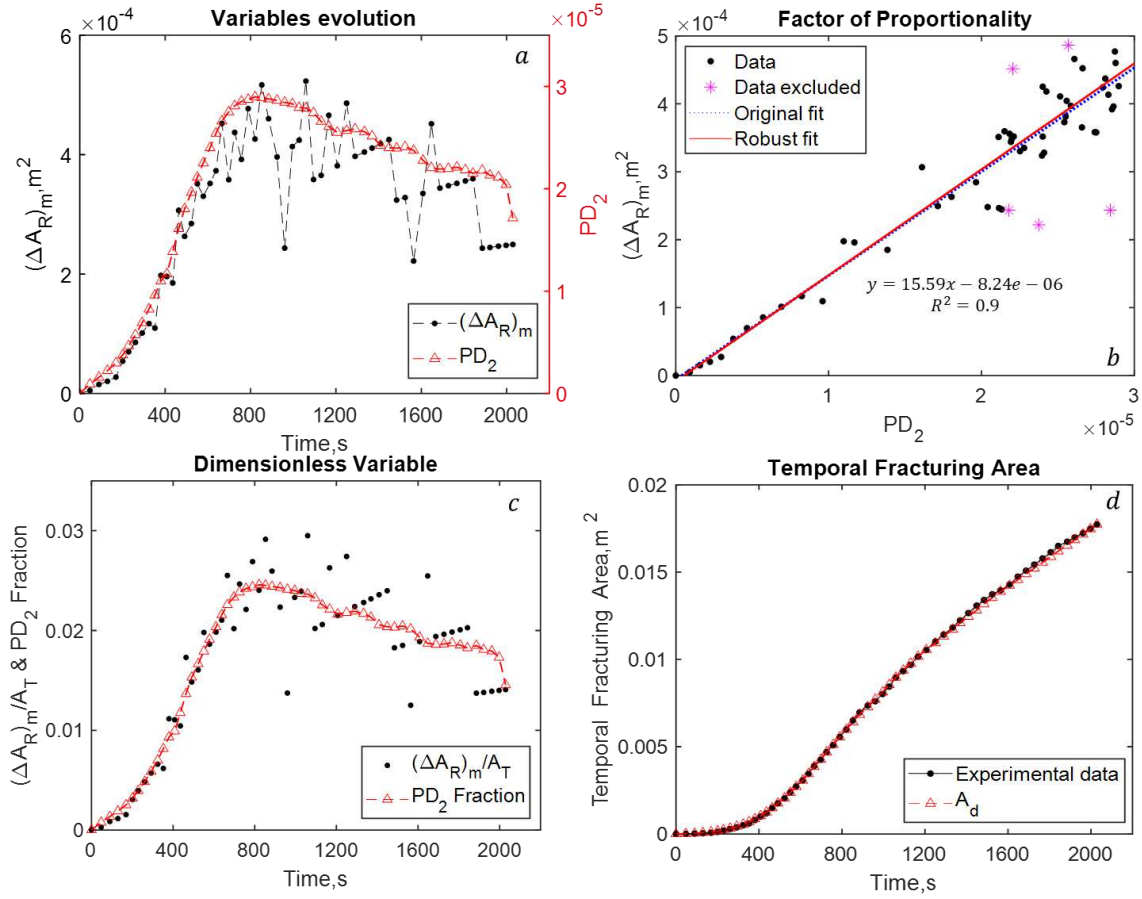


Fig.5 Evolution of the fracture area for the Colton 08 sandstone sample during stable propagation; Comparison between direct laboratory measurements and predictions of the new model presented here.

3.3.2 Unstable fracture propagation (no leak-off)

Here we validate the model of fracturing area A_d for an unstable propagation using published data detailed in Section 3.1, i.e., **Colton 09** and **c11m1** samples for which no leak-off is expected.

Colton 09 and c11m1:

The evolution of the fracture area with time measured by Lhomme (2005) in the Colton 09 sample, and by Bungler et al. (2013) in the PMMA sample c11m1, along with the predictions of the new A_d model are shown in **Figs. 6 and 7**, respectively. Analogously to the case of stable propagation, we obtain reasonably good linear correlations, i.e.,

$$(\Delta A_R)_m = 0.14 * \sqrt[3]{-\frac{w_m^2}{12\mu_f} \left(\frac{\Delta p_o}{\Delta t}\right)_m} - 2.28e - 07, \text{ with } R^2 = 0.95 \quad (35)$$

for the Colton 09 sample, and

$$(\Delta A_R)_m = 1.35 * \sqrt{-\frac{w_m^2}{12\mu_f} \left(\frac{\Delta p_o}{\Delta t}\right)_m} - 1.37e - 08, \text{ with } R^2 = 0.92 \quad (36)$$

for the PMMA c11m1 sample.

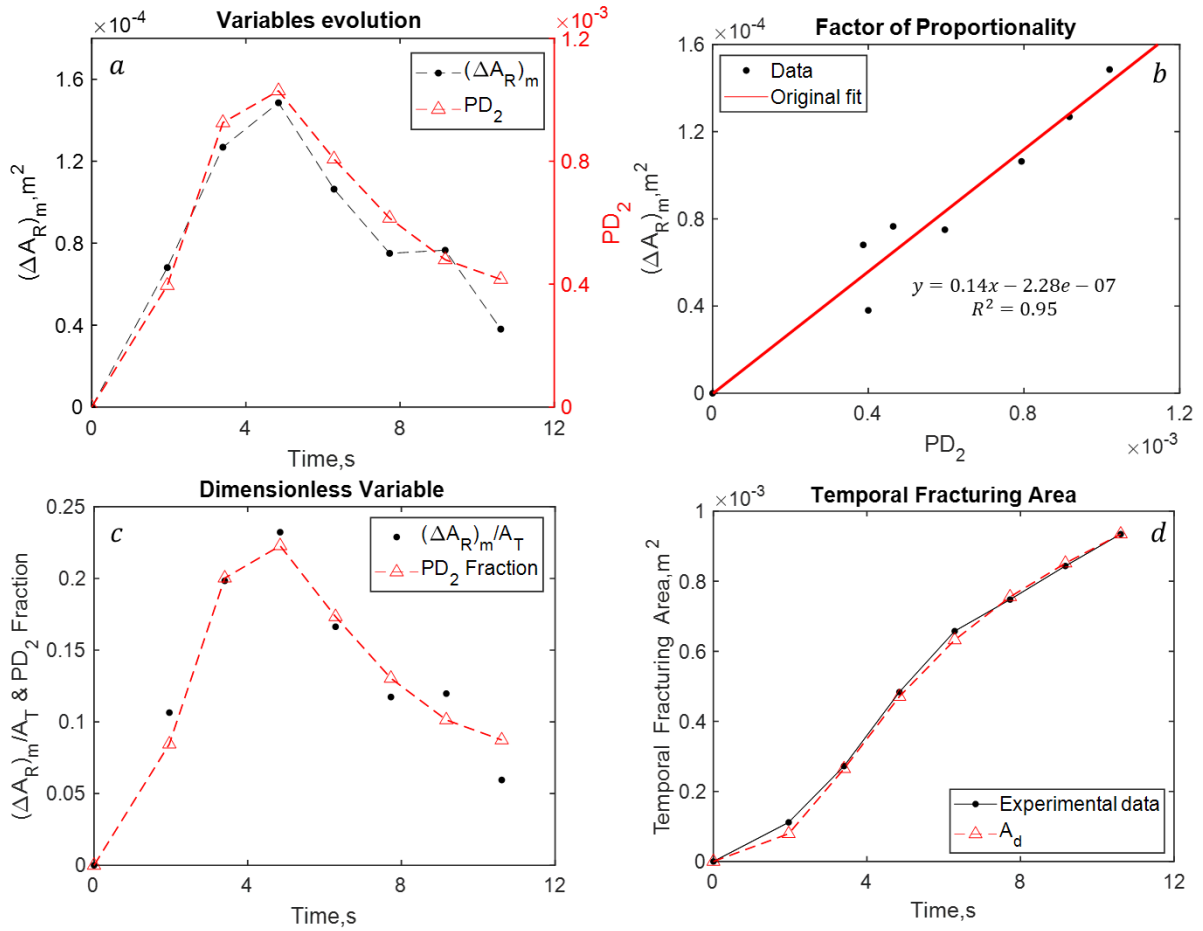


Fig.6 Evolution of the fracture area for the Colton 09 sandstone sample during unstable propagation; Comparison between direct laboratory measurements and predictions of the new model presented here.

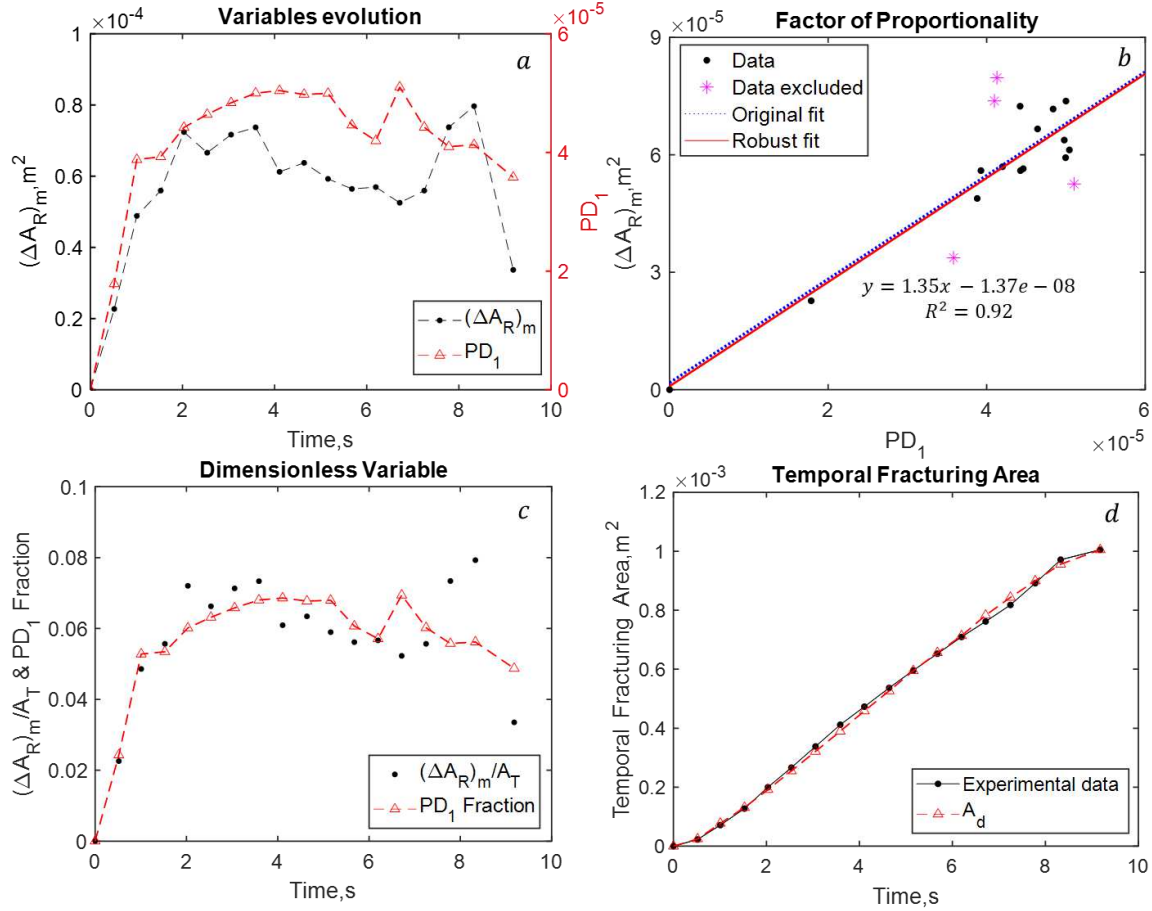


Fig.7 Evolution of the fracture area for the PMMA sample c1 l m l during unstable propagation; Comparison between direct laboratory measurements and predictions of the new model presented here.

4. Comparison between fracturing models

For the seven samples detailed in **Table 3**, we compare here the radius predictions of (i) the asymptotic solutions, i.e., viscosity-driven R_V in **Eq.28**, and toughness-driven R_T in **Eq.29**; (ii) the linear elastic fracture model R_E in **Eq.7**; and (iii) the new self-similar fracture growth R_d in **Eqs.21 and 24**, or **23 and 24**, depending on whether cohesive-zone effects are significant.

4.1 Stable fracture propagation

4.1.1 Without leak-off

We report here the comparison between the model predictions and the experimental data for the cement/sand sample **Cov12c** (viscosity-dominated fracture propagation experiment), and one ultra-tight sandstone sample **Colton 08** (toughness-dominated fracture propagation experiment). The time evolution of the fracture radius as predicted by the four models R_V , R_T , R_E and R_d are compared to the experimentally-estimated radius in **Fig.8**.

For both samples **Cov12c (Fig.8a)** and **Colton 08 (Fig.8b)**, the predicted radius R_d agrees well with experimental data for the entire propagation period. For sample **Cov12c (Fig.8a)**, the predicted radius R_E slightly over-estimates the measured fracture radius at early time ($T < 200s$), but slightly under-estimates it when $t > 400 s$. For **Colton 08 (Fig.8b)**, the predicted radius R_E is in relatively good agreement with experimental data when $T < 600 s$, but significantly overestimates the measured fracture radius after 600 s. The radius predicted by the asymptotic solutions R_V and R_T (viscosity- and toughness-driven, respectively) significantly overestimates the experimental measurements, although this discrepancy fades with time, i.e., $t > 500 s$.

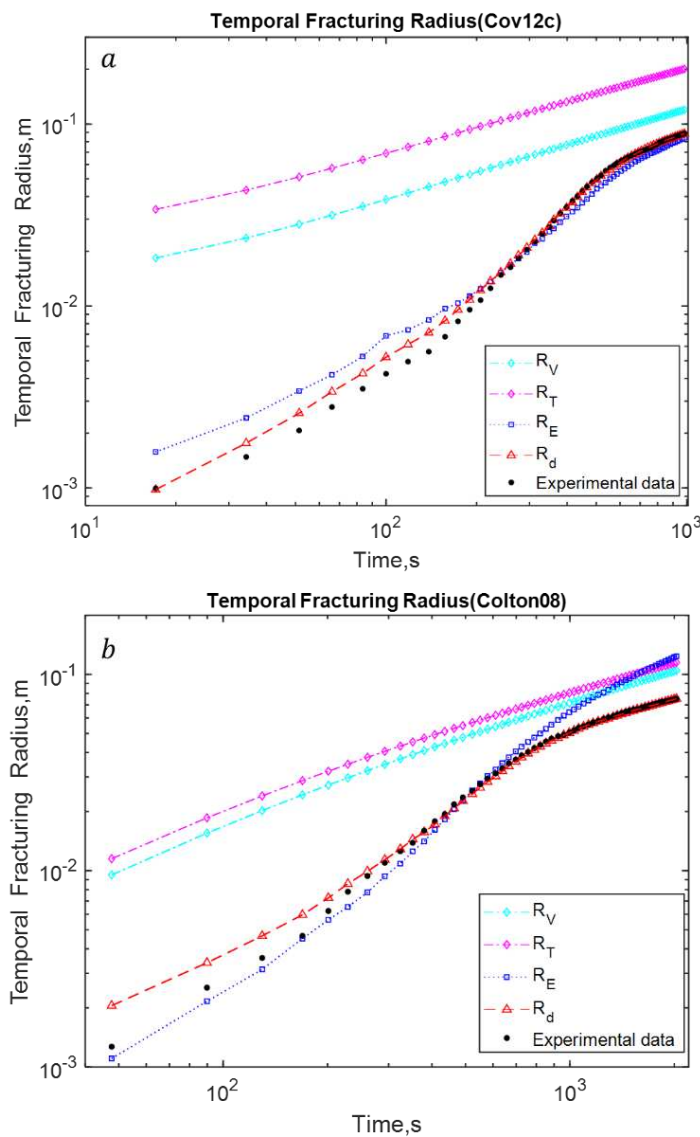


Fig.8 History match of experimental fracturing radius based on asymptotic solution (R_V and R_T), elasticity theory (R_E), and R_d models: a) Cov12c; b) Colton 08

4.1.2 With leak-off

We report here the comparison between the model predictions and the experimental data for the **Felser 02** sample (**Fig.9**). The predicted radius R_d matches well the experimental data except at early propagation time (i.e., $t < 300$ s), whereas the predicted R_E slightly underestimates the measured radius for the entire propagation time. On the other hand, R_V and R_T significantly over-estimate the experimental data at all times during the hydraulic fracturing experiment. Fluid loss (leak-off) through the fracture's wall during fracturing is a plausible cause for the smaller fracture radius reached at a given time during fracture propagation compared to the predictions of the asymptotic solution (Lhomme 2005). The large-time trend for all models is similar, but the asymptotic solution neglecting leak-off exhibits an offset of about one order of magnitude.

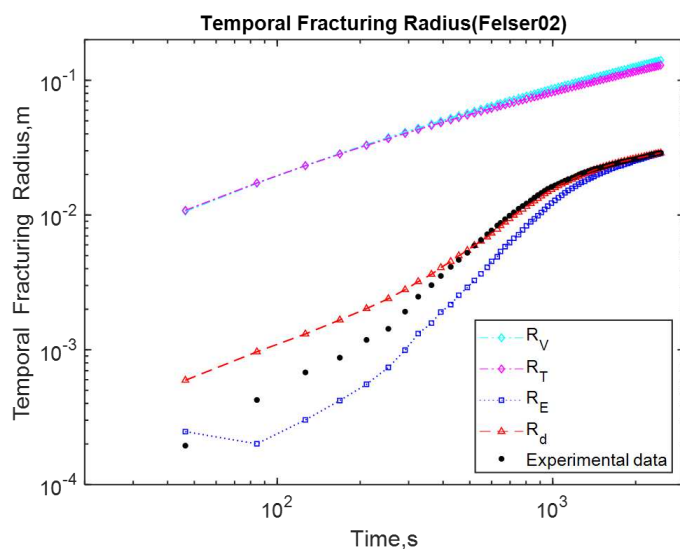


Fig.9 History match of experimental fracturing radius based on asymptotic solution (R_V and R_T), elasticity theory (R_E), and R_d models: Felser 02

In summary, for a stable fracture propagation (**Figs.8 and 9**), we observe a better agreement between the R_d model predictions and the experimental data compared to the other two models. Overall, the discrepancies between model and data fade at large time (except for the R_E of **Colton08**), and the large-time trends are approaching to be consistent between data, models, and asymptotic solutions.

4.2 Unstable fracture propagation

We report here the comparison between the model predictions and the experimental data for the ultra-tight sandstone sample **Colton 09** (viscosity-dominated fracture propagation experiment), the two PMMA samples **ab5** and **c11m1** (toughness-dominated fracture

propagation experiment) on one hand, and the tight sandstone sample **Felser 03** (toughness-dominated fracture propagation experiment) on the other. The time evolution of the fracture radius as predicted by the four models R_V , R_T , R_E , and R_d are compared to the experimentally-estimated radius in **Figs. 10 and 11**.

4.2.2 Without leak-off

For the three samples (**Fig.10**), the propagation time is only about 10 seconds to reach a final radius of approximately 0.02m. The R_d model predictions agree well with experimental data. In terms of the consistency, the R_T model predictions show the effectiveness for the PMMA samples (**Fig.10b and c**), but exhibit moderate discrepancies for the **Colton09** sample (**Fig.10a**). However, the predicted R_E radius significantly deviates from the experimental measurements even at the large time for these three samples.

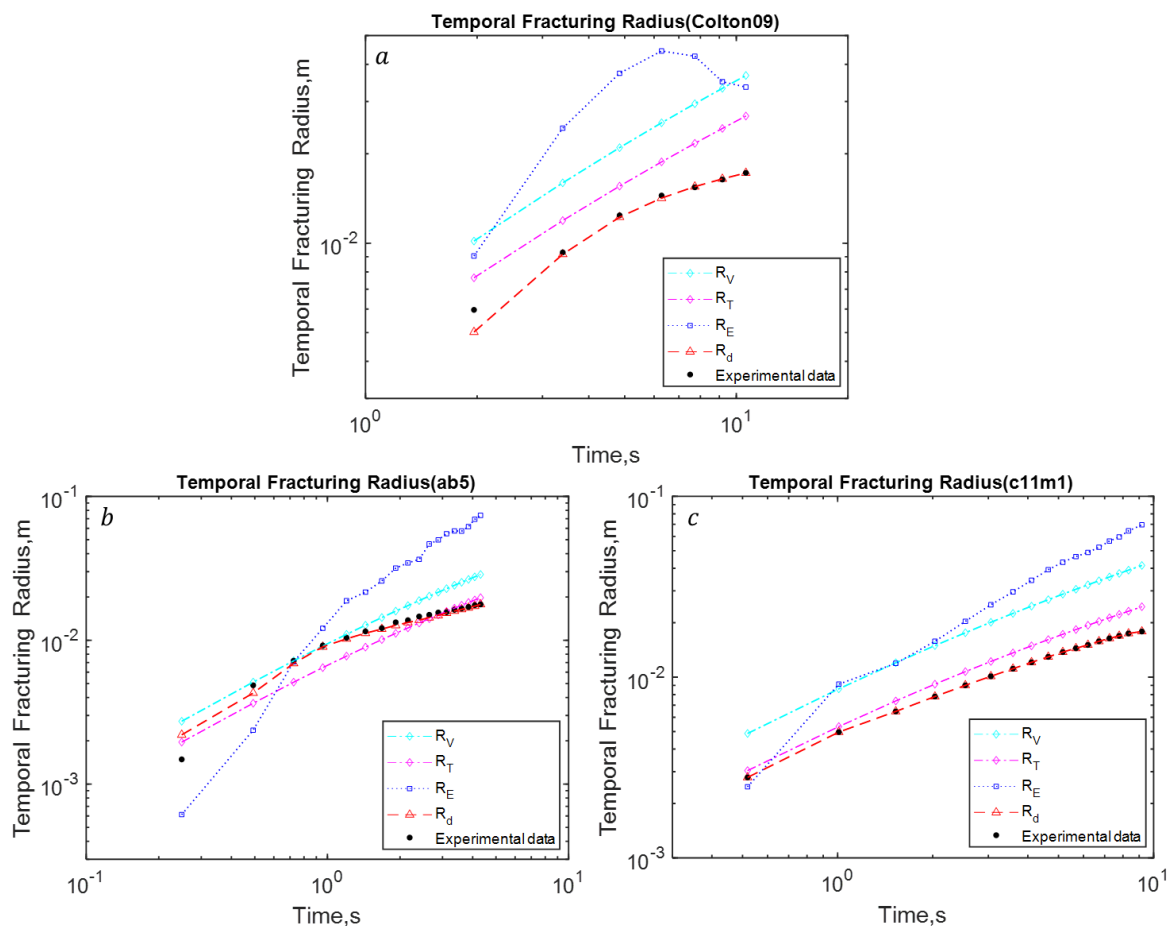


Fig.10 History match of experimental fracturing radius based on asymptotic solution (R_T), elasticity theory (R_E), and R_d model: a) Colton 09; b) ab5; c) c11m1

4.2.3 With leak-off

For the **Felser 03** sample (**Fig.11**), the R_d predictions agree well with experimental data. On the other hand, the R_E model slightly under-estimates the experimental data at early time, but

becomes more effective at large time. The predictions based on R_V and R_T model significantly over-estimate the experimental radius at all times.

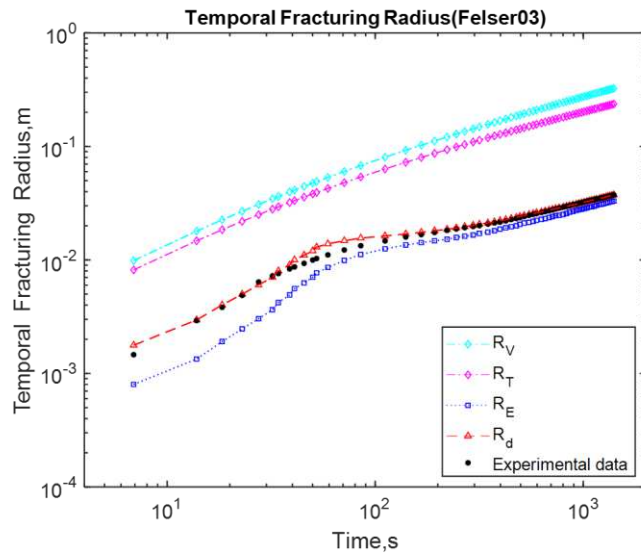


Fig.11 History match of experimental fracturing radius based on asymptotic solution (R_T), elasticity theory (R_E), and R_d model, and experimental data- Felser 03.

In summary, for unstable fracture propagation, the R_d model predictions compare well with experimental data, whereas the R_E model is significantly less effective for the **Colton 09** and two **PMMA**s. On the other hand, the asymptotic solution (R_T model) is effective for the toughness-dominated fracturing experiments with the **PMMA** samples, but clearly inadequate for sandstone samples **Colton 09**, and **Felser 03**, regardless of leak-off.

5. Discussion and Implications

5.1 Incremental increase in fracture area $(\Delta A_R)_m$

The linearity between $(\Delta A_R)_m$ and PD (involving the pressure change with time at the fracture inlet/borehole) is an important indicator of a successful R_d model. For both stable and unstable fracture propagation without leak-off, this linearity is evident, resulting in a good agreement of the model with experimental data for most samples for which direct measurement of the fracture radius evolution with time is available in the literature (see Tables 3 and 4, and **Figs. 4b, 5b, 6b, 7b, and A2b**). On the other hand, when leak-off effects play a role in relatively permeable samples, e.g., Felser 02 in **Fig.B1b** and Felser 03 in **Fig.B3b**, the linear regression between $(\Delta A_R)_m$ and PD is less robust, resulting in slight discrepancy between R_d predictions and experimental data. This also supports the linearity between the time-change in fluid

pressure at the fluid front and the time-change in wellbore/inlet pressure at each propagation increment (**Fig.A1**), i.e., $\left. \frac{\partial p_f(r,t)}{\partial t} \right|_{r=R_f} \propto \left(- \left. \frac{dp_f(r,t)}{dt} \right|_{r=0} \right)$.

Porosity may also affect the aforementioned relationship; the more porous the rock, the more irreversible deformation is recorded during hydraulic fracturing according to Holt et al. (2015) or Wong and Baud (2012) for instance. This is qualitatively consistent with the set of samples with different porosity we used in this study, i.e., in the Felsers 02 and 03 sandstone samples ($\Phi = 0.21$), the Colton sandstone ($\Phi = 0.12$), and the cement/sand composite Cov12c ($\Phi = 0.15$).

5.2 Validity of the Poiseuille flow within hydraulic fracture

Based on the comparison between fracturing models we conducted here (**Sections 3.3 and 4**), we confirm that the near-tip cohesive zone plays a critical role during the propagation of a hydraulic fracture in conventional rocks having a tensile strength in the rang 2 to 12 MPa when in situ stress conditions at depth induce a high σ_o/σ_c ratio. In the viscosity-dominated propagation regime with significant fluid lag (Cov12c), and where the cohesive zone is embedded in the lag zone (see **Fig.1b**), the conventional Poiseuille flow law is shown to be acceptable (**Fig. 4b**). In contrast, when a relatively small fraction of fluid lag is embedded in the cohesive zone (**Fig.1c for Colton 08 and 09**), the proportionality between width w and fluid velocity u must be modified to a fractional power dependence $w \propto \left(\frac{dR}{dt} \right)^{\frac{3}{2}}$, see **Figs. 5b and 6b**. For materials like PMMA with a relatively higher tensile strength (above 60MPa), the impact of the cohesive zone on fracture propagation is very limited, which in turn suggests that the conventional Poiseuille flow law and Linear elastic fracture mechanics (LFEM) can be used under such conditions **Fig.7b**.

5.3 Applicability of the R_v , or R_T , R_E , and R_d models

The results indicate that the fracture radius predictions based on the asymptotic solutions (R_v or R_T) are only suitable for linearly elastic homogeneous materials, i.e. PMMA (**Fig.10b and c**), with significant deviation observed in the synthetic/natural tight sandstones tested (i.e., Cov12c, Coltons, and Felsers). The prediction performance of the linear elastic model (R_E) is poor for unstable propagation cases (**Fig.10**). Although it shows partial agreement with the data in some cases (**Figs.8 and 11**), the simplification of the fluid pressure distribution P_f within the fracture (i.e., **Eq.9**) leads to unreliable predictions.

The results also show that the new R_d model matches well the experimental data, regardless of the propagation regimes; the stability of the propagation; or whether leak-off is significant. The only consideration is the early-time overestimation of R_d in the stable case with leak-off (**Fig.10**). Such a broad applicability is due to the fact that this model is based on a mechanistic approach and involves self-similar growth, dimensional analysis, and direct laboratory observations. This suggests that the R_d model can be robustly applied in the laboratory. It is also probably applicable in the field by extrapolation, which remains to be explored.

7. Conclusion and Recommendations

Hydraulic fracture propagation is a complex and coupled process involving fluid-solid interactions, integrating multiscale propagation regimes with stability conditions to be accounted for under varying stress regimes (e.g., depth, proximity to major tectonic faults, etc.). This significantly challenges our ability to predict/control the propagation of hydraulic fractures, and the fate of fracturing fluids underground.

We thus compare here several models for the prediction of the time-evolution of the radius of penny-shaped fracture at depth. The first model relies on linear elastic fracture mechanics (R_E); the second is based on the Poiseuille's flow law within the fracture and on the assumption of self-similar fracture growth (R_d); and the third and fourth are the viscosity-driven or toughness-driven asymptotic fracturing models (R_v and R_T). Their applicability is assessed against published experimental data, i.e., hydraulic fracturing of five synthetic/natural tight sandstone samples under true tri-axial stress, and two PMMA samples under biaxial stress conditions.

The results show that the cohesive zone plays an important role in hydraulic fracturing for conventional rocks ($2 \leq \sigma_c \leq 12\text{MPa}$): (i) Poiseuille flow within the fracture is valid for propagation in the viscosity-dominated regime ($k \ll 1$) with significant fluid lag ($\Psi \gg 1$); and (ii) when a small fluid lag is embedded within the cohesive zone (**Fig.1c**), the proportionality

$w \propto \frac{dR}{dt}$ must be modified to $w \propto \left(\frac{dR}{dt}\right)^{\frac{3}{2}}$ in the R_d model.

The asymptotic models are limited to linearly elastic homogeneous materials, i.e. PMMA (**Fig.10b and c**). The (R_E) model poorly agrees with the experimental data, especially for unstable propagation cases. On the other hand, a good agreement between the results from our R_d model and experimental data indicates that the experimental radius of the hydraulic fracture under true tri-axial stress condition can be properly reconstructed:

- (i) The self-similar propagation of radial hydraulic fractures is valid for laboratory-scale experiments.
- (ii) Where fracture aperture, wellbore pressure, and the boundaries are obtained from laboratory or field investigations, our R_d model can predict the fracture radius evolution with time in multiple situations (e.g., stable/unstable propagation, leak-off effect). The model is mathematically simple to implement with low computational costs.
- (iii) Field assessment of the R_d model is recommended, where the radius predicted from R_d can be applied for the calibration of fracture growth monitoring based on active/passive seismic data interpretation.

Declaration of competing interest

The authors declare that they have no known competing interest

Acknowledgments

The first author sincerely thanks China Scholarship Council- Curtin International Postgraduate Research Scholarship (CSC-CIPRS, Grant No. 201808190001) for their financial support on this research.

Appendix A: Mathematic transformation (Eq.13) and the validation of hypothesis (Eq.14)

A.1. Derivation of equation (10)

The total derivative of fluid pressure $p_f(r,t)$ as function of time t can be written as:

$$\frac{dp_f(r,t)}{dt} = \frac{\partial p_f(r,t)}{\partial r} \frac{\partial r}{\partial t} + \frac{\partial p_f(r,t)}{\partial t} \frac{\partial t}{\partial t}, \text{ with } 0 < r < R_f < R. \quad (\text{A1})$$

At $r = R_f(t)$, Eq.(A1) can be rewritten as

$$\left. \frac{dp_f(r,t)}{dt} \right|_{r=R_f(t)} = \left. \frac{\partial p_f(r,t)}{\partial r} \right|_{r=R_f(t)} \frac{dR_f(t)}{dt} + \left. \frac{\partial p_f(r,t)}{\partial t} \right|_{r=R_f(t)} \quad (\text{A2})$$

At any time, at fluid front $r = R_f(t)$ a lag with the fracture tip exists, where the pressure is essentially zero (if not negative and cavitation can occur); thus, at all times during fracture propagation $\left. \frac{dp_f(r,t)}{dt} \right|_{r=R_f(t)} \cong 0$, and Eq.(A2) becomes

$$\left. \frac{\partial p_f(r,t)}{\partial r} \right|_{r=R_f(t)} \frac{dR_f(t)}{dt} + \left. \frac{\partial p_f(r,t)}{\partial t} \right|_{r=R_f(t)} \cong 0 \quad (\text{A3})$$

Combining Eq.(A3) and Eq.(10) in the main text yields

$$\left(\frac{dR_f(t)}{dt}\right)^2 \cong \frac{w^2}{12\mu_f} \left.\frac{\partial p_f(r,t)}{\partial t}\right|_{r=R_f(t)} \quad (\text{A5})$$

A.2. Assumption on the fluid pressure time derivatives

Eq.(A5) requires the knowledge of the partial derivative of the fluid pressure near the fluid front in a propagating hydraulic fracture $\left.\frac{\partial p_f(r,t)}{\partial t}\right|_{r=R_f(t)}$. This data is often inaccessible in practice, neither in the laboratory nor in the field. The key accessible parameter is the wellbore pressure, corresponding essentially to the fluid pressure at the inlet of the fracture.

Based on the few evaluations of fluid pressure profiles along a propagating hydraulic fracture available in the literature, we hypothesise that at each time increment, the change with time in fluid pressure at the fluid front $\left.\frac{\partial p_f(r,t)}{\partial t}\right|_{r=R_f(t)}$ is linearly related to the change with time of the fluid pressure at the fracture inlet (wellbore) $\left.\frac{\partial p_f(r,t)}{\partial t}\right|_{r=0}$, with a time-dependent proportionality coefficient $-\lambda_p(t)$, assumed to be time-dependent for generality (see **Fig.A1**). Noting that at the borehole $r = 0$

$$\left.\frac{\partial p_f(r,t)}{\partial t}\right|_{r=0} = \frac{\partial p_f(0,t)}{\partial t} = \frac{dp_o(t)}{dt}, \quad (\text{A6})$$

where $p_o(t)$ is the borehole/injection pressure, we obtain **Eq.(11)** in the main text, i.e.,

$$\left.\frac{\partial p_f(r,t)}{\partial t}\right|_{r=R_f} = -\lambda_p(t) \frac{dp_o(t)}{dt}, \quad (\text{A7})$$

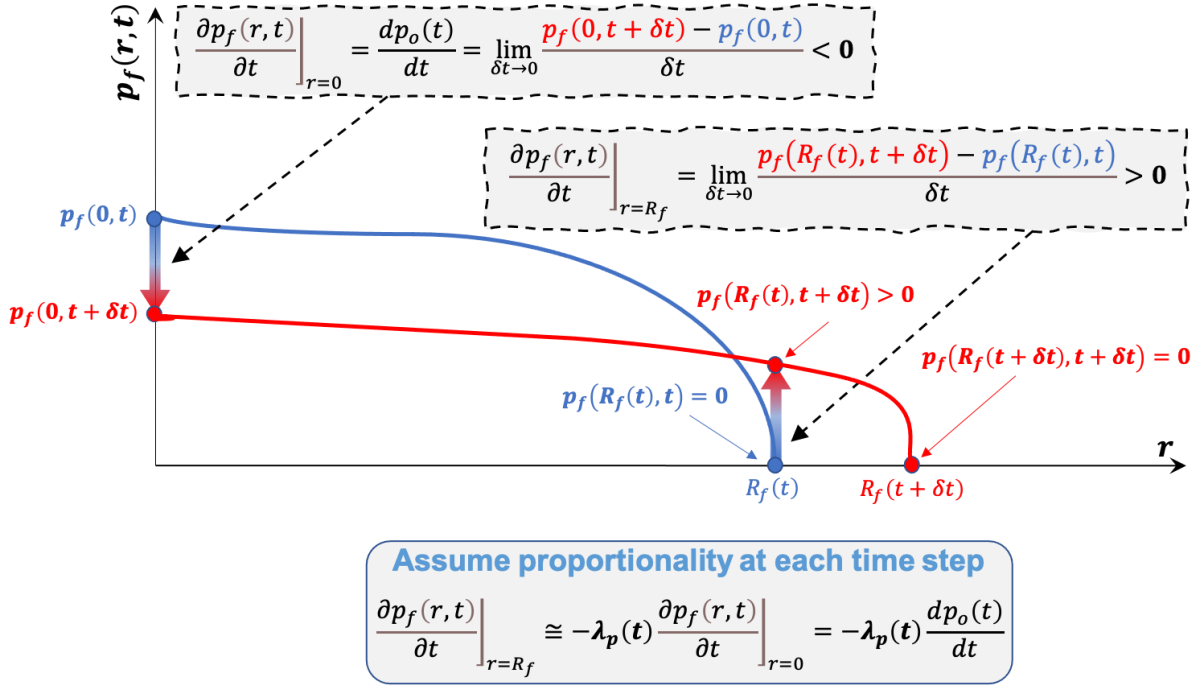


Fig.A1. Schematic justification of the hypothesis on the fluid pressure time derivatives at the inlet and tip of a propagating hydraulic fracture.

A.3. Validation of the assumption on the fluid pressure time derivatives

To validate **Eq.(11)** recalled above, we use the few model predictions of fluid pressure profiles within a propagating penny-shaped hydraulic fracture (Kanaun 2018 and 2020; Zia and Lecampion 2020). Estimating the time derivatives of the fluid pressure at the inlet and near the tip of a propagating hydraulic fracture we can estimate the proportionality coefficient $-\lambda_p(t)$ for the various time steps reported in each publication (see **Fig.A2**). It turns out that λ_p is approximately fixed for a given fracture propagation simulation (see **Fig.A3**), which corresponds to **Eq.(12)** in the main text, i.e., $\left. \frac{\partial p_f(r, t)}{\partial t} \right|_{r=R_f(t)}$ is approximately linearly related to $\frac{dp_o(t)}{dt}$ during fracture propagation.

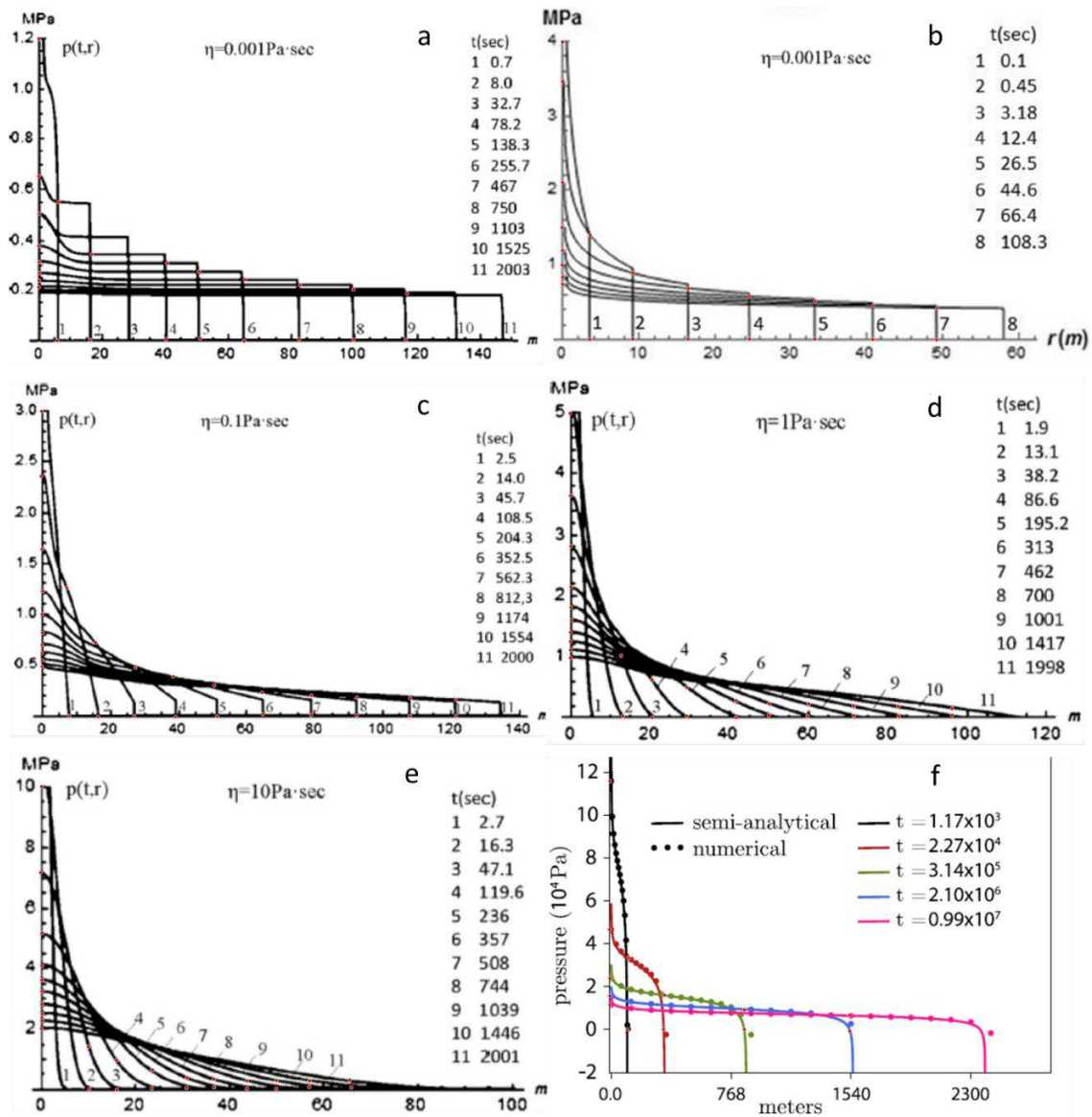


Fig.A2. Fluid pressure $P_f(r,t)$ distribution within a penny-shaped hydraulic fracture: (a)-(e) from Kanaun (2018 and 2020); (f) from Zia and Lecampion (2020)

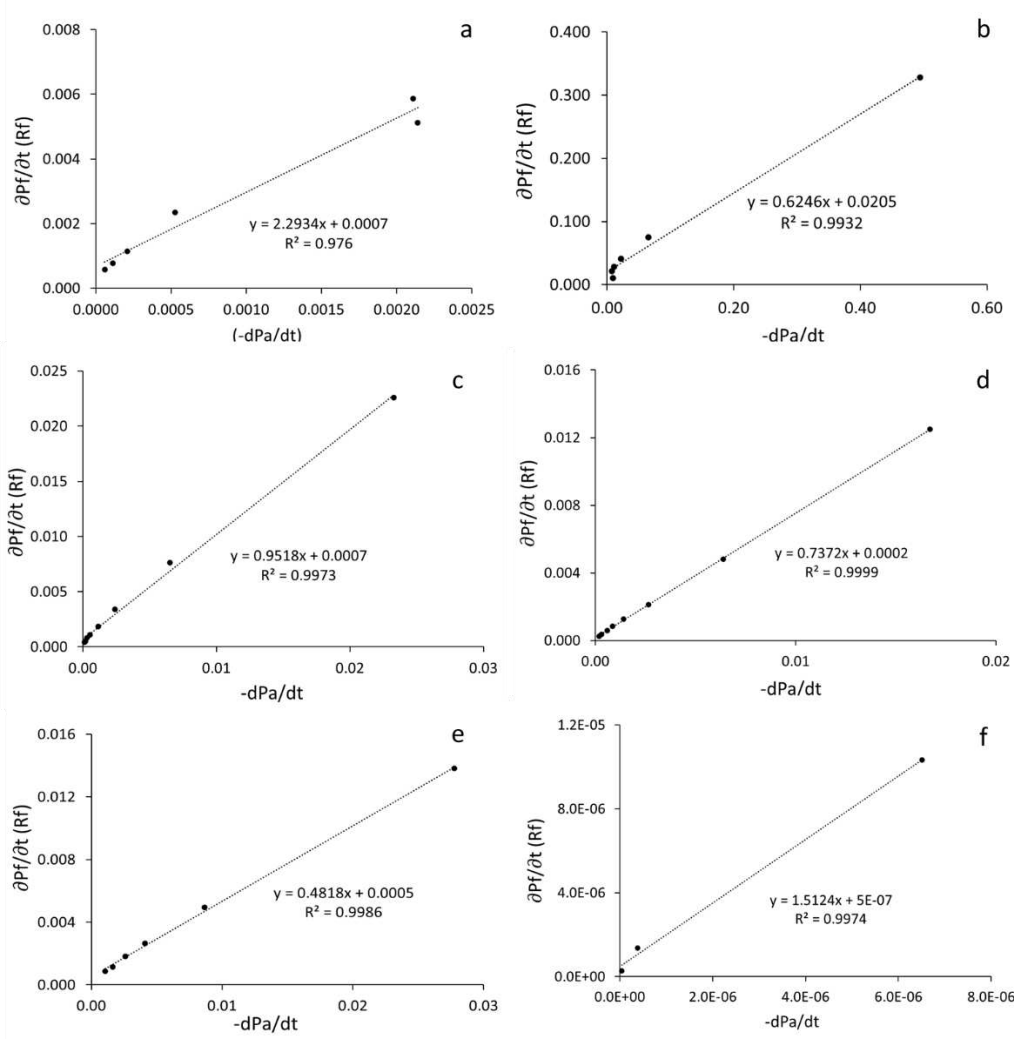


Fig.A3. Validation of Eq.12 using literature data for a penny-shaped hydraulic fracture: (a)-(e) from Kanaun (2018 and 2020); (f) from Zia and Lecampion (2020).

Appendix B: $\frac{dp_o}{dt}$ Correction for early-time initiation

When the process of early-time fracture initiation is significant, i.e., the fracture initiates at a much lower wellbore pressure than the breakdown pressure (i.e. maximum pressure recorded during the entire test), which is mostly happened in stable propagation cases, e.g., hydraulic fracturing tests reported in Lhomme (2005), Sarmadivaleh (2012), and Lecampion et al. (2017). Therefore, the pressurization rate ($\frac{dp_o}{dt}$) stay positive until reaches to the breakdown pressure,

for convenience of calculating the *product* $PD \sqrt{-\frac{w^2}{12\mu_f} \frac{\Delta p_o}{\Delta t}}$, the pressurization rate for early-time fracture propagation ($\frac{\Delta p_o}{\Delta t}_{ei}$) can be corrected as:

$$\frac{\Delta p_o}{\Delta t}_{ei} = \frac{\Delta p_o}{\Delta t} - \frac{\Delta p_o}{\Delta t}_{pri} \quad (B1)$$

where $\frac{\Delta p_o}{\Delta t}_{pri}$ is the linearized wellbore pressurization rate before fracture initiation.

For stable propagation case (i.e., significant early-time initiation & propagation), the correction of $\frac{\Delta p_o}{\Delta t}$ will be only applied prior to maximum wellbore pressure. On the other hand, for unstable propagation case where the initiation and breakdown of wellbore pressure always coincide, the effective pressurization rate ($\frac{\Delta p_o}{\Delta t}_{ei}$) will be used for the entire propagation due to the wellbore storage effect (Lecampion et al. 2017).

Appendix C: Temporal fracturing area (A_d) validation for leak-off and repeated case

C.1. Felser 02: Stable propagation case with leak-off

The evolution of the fracture area with time measured by Lhomme (2005) in Felser 02 is displayed in **Fig.C1**. Similar to Colton 08, the cohesive zone effect are also necessarily accounted. As shown in **Fig.C1a**, the $(\Delta A_R)_m$ exhibited reasonably analogous trend with the $product_2 (PD_2) \sqrt[3]{-\frac{w_m^2}{12\mu_f} \left(\frac{\Delta p_o}{\Delta t}\right)_m}$, albeit stronger fluctuation of $(\Delta A_R)_m$ is observed after the peak. The robust linear regression analysis of $(\Delta A_R)_m$ verse PD_2 indicates a weakly linear relation with $R^2 = 0.84$ (**Fig.C1b**):

$$(\Delta A_R)_m = 3.07 * \sqrt[3]{-\frac{w_m^2}{12\mu_f} \left(\frac{\Delta p_o}{\Delta t}\right)_m} + 1.79 \times 10^{-6} \quad (C1)$$

The time evolution of the dimensionless relative change in experimental fracture area

$$(\Delta A_R)_m / A_T \text{ and the analytical fraction } \frac{\sqrt[3]{-\frac{w_m^2}{12\mu_f} \left(\frac{\Delta p_o}{\Delta t}\right)_m}}{\sum_{i=1}^N \sqrt[3]{-\frac{w_i^2}{12\mu_f} \left(\frac{\Delta p_o}{\Delta t}\right)_i}} \text{ are shown in}$$

Fig.C1c, indicating a reasonably robust fit, despite some fluctuations in measured $(\Delta A_R)_m / A_T$.

Finally, **Fig.C1d** compares the predicted evolution of the fracturing area A_d (red triangle) and the experimental data (black dots), validating the hypothesis and approach followed here.

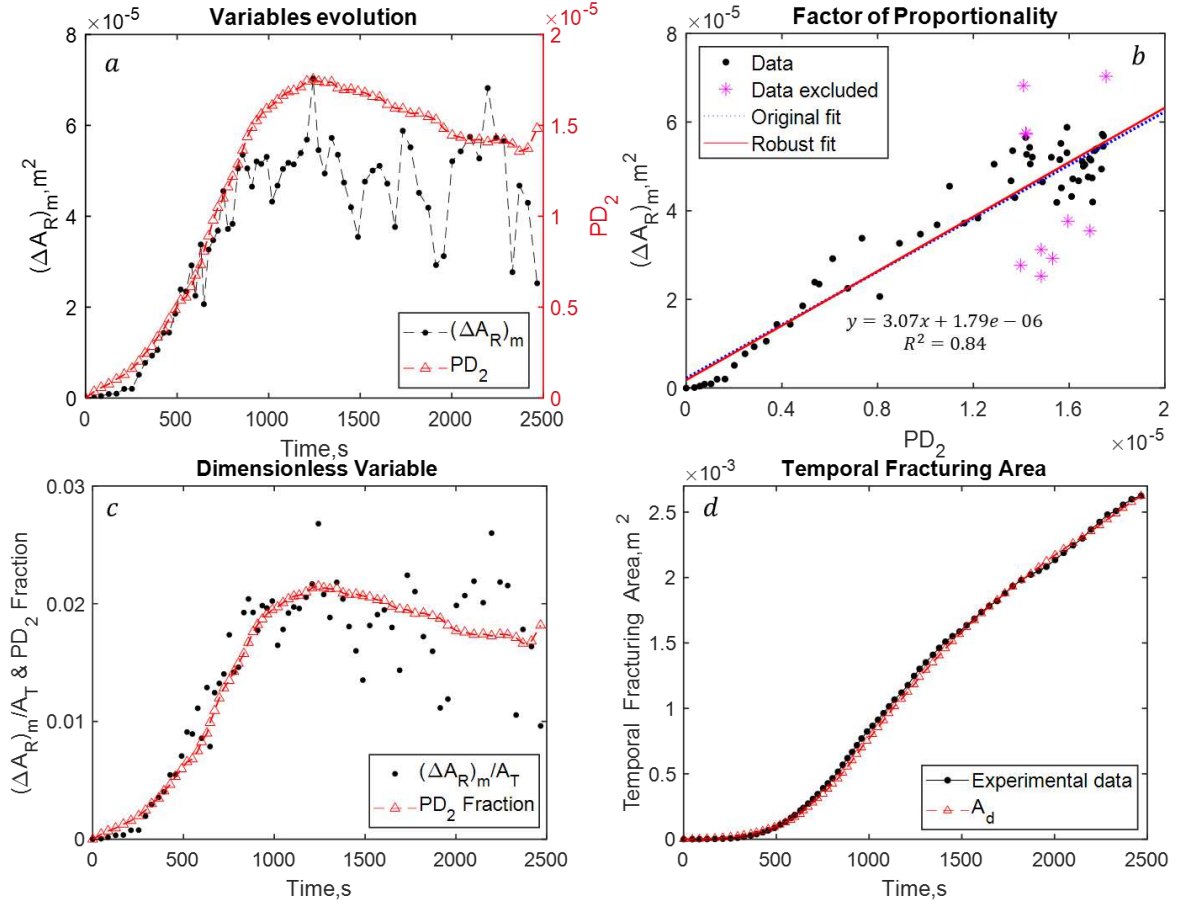


Fig.C1 Evolution of the fracture area for the Felser 02 sandstone sample during stable propagation: Comparison between direct laboratory measurements and predictions of the new model presented here.

C.2. ab5: Unstable propagation case(no leak-off)

The evolution of the fracture area with time measured by Bungert et al. (2013) in ab5 and the prediction from our A_d model are shown in **Fig.C2**. Analogously to the previous PMMA case(c11m1), we obtain the reasonably good linear correlation **Fig.C2b**:

$$(\Delta A_R)_m = 2.9 * \sqrt{-\frac{w_m^2}{12\mu_f} \left(\frac{\Delta p_o}{\Delta t}\right)_m} - 3.07e - 06, \quad R^2 = 0.93 \quad (C2)$$

Accounting for these correlations, **Fig.C2d** show the final results for the two corresponding samples. Again, a reasonable fit is found between predicted and measured evolution of the fracture area, although the minor discrepancy is observed during the intermediate propagation time.

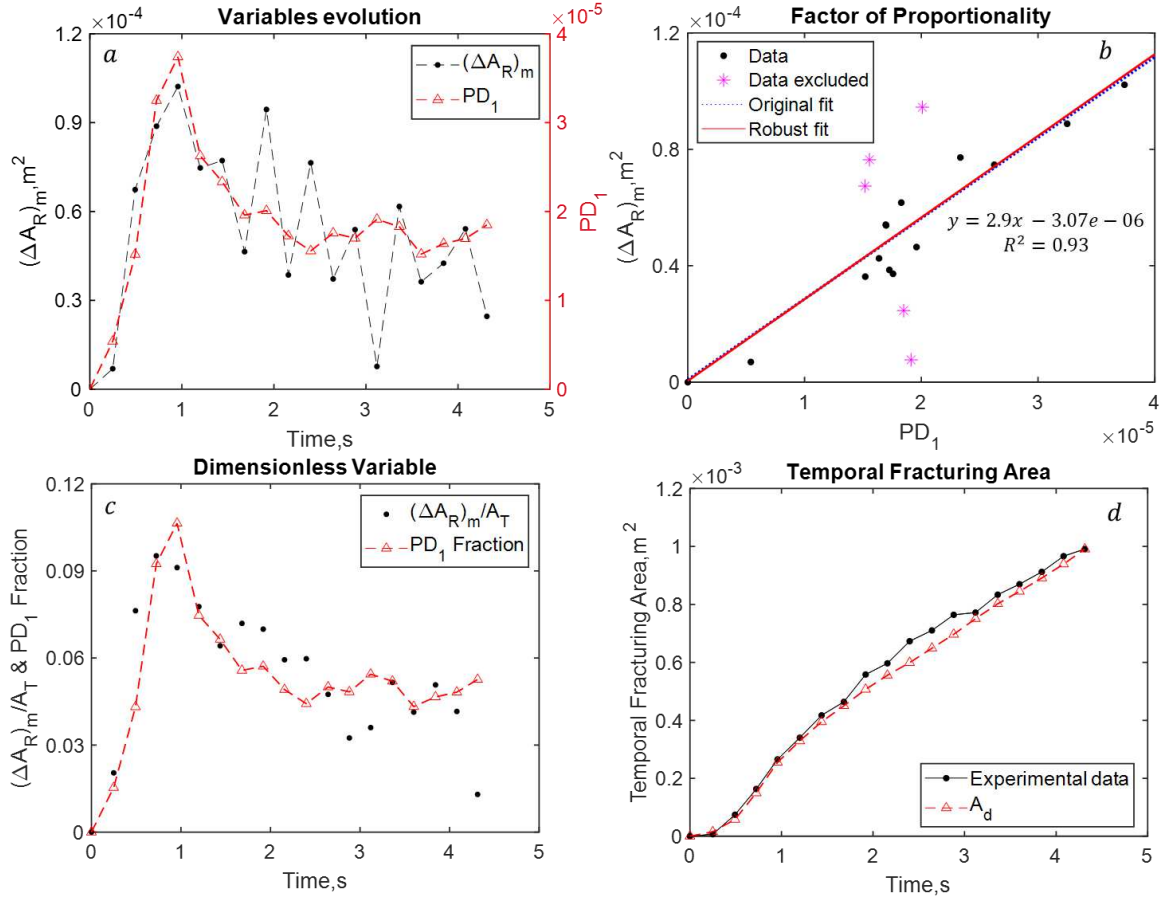


Fig.C2 Evolution of the fracture area for the ab5 (PMMA sample) during stable propagation: Comparison between direct laboratory measurements and predictions of the new model presented here.

C.3. Felser 03: Unstable propagation case with leak-off

Unlike the unstable cases with non-leak-off (i.e., Colton 09, ab5, and c11m1), for Felser 03 the value of $(\Delta A_R)_m$ significantly scatter after propagation of 50s (**Figs.C3a**), resulting in a weak linearity between $(\Delta A_R)_m$ and PD_2 (**Fig.C3b**) :

$$(\Delta A_R)_m = 7053 * \sqrt[3]{-\frac{w_m^2}{12\mu_f} \left(\frac{\Delta p_o}{\Delta t}\right)_m} - 9.1e - 07, R^2 = 0.76 \quad (C3)$$

The linear regression analysis indicates that the proportional hypothesis between $(\Delta A_R)_m$ and PD_2 is partially valid; the value of y-axis intercept B are still negligible since $B \ll (\Delta A_R)_m$. Although the dimensionless variable $(\Delta A_R)_m/A_T$ are highly fluctuated after 50s (**Fig.C3c**), the temporal fracturing area (A_d) are in relatively good agreement with the experimental data.

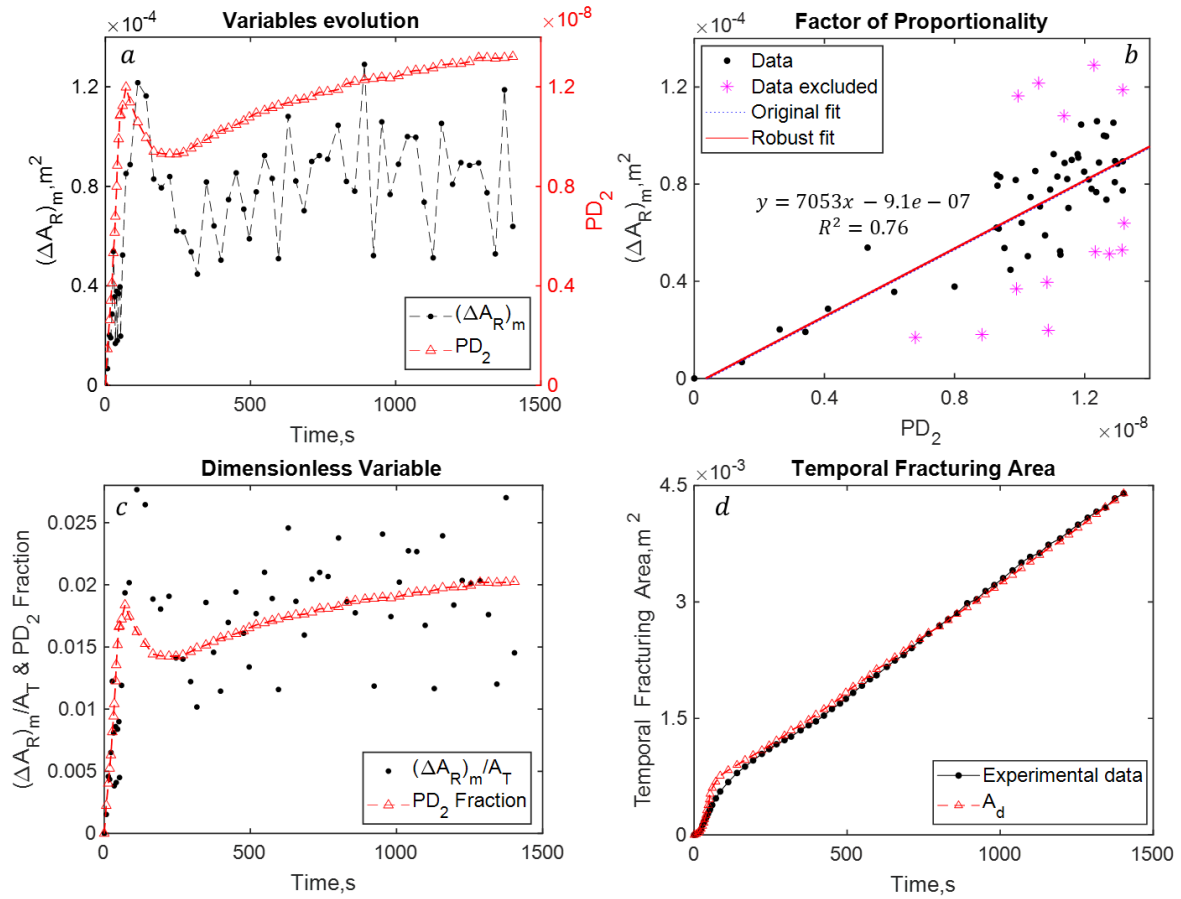


Fig.C3 Evolution of the fracture area for the Felser 03 during stable propagation: Comparison between direct laboratory measurements and predictions of the new model presented here.

Abbreviations

<i>TTSC</i>	True tri-axial stress condition
<i>TTSCs</i>	True tri-axial stress cell
<i>UCS</i>	Uniaxial compressive strength
<i>TCS</i>	Tri-axial compressive strength
<i>BHP</i>	Wellbore pressure
<i>PMMA</i>	Polymethyl Methacrylate
<i>LEFM</i>	Linear Elastic Fracture Mechanics
<i>md</i>	MiliDracy

List of Symbols

Q_o	Constant injection rate supplied by pump
q	Flow rate per unit perimeter
P_f	Fluid pressure
P_b	Breakdown pressure
P_o	Wellbore pressure
u	Fluid velocity
<i>BHP</i>	Wellbore pressure
w	Width of hydraulic fracture
A_R	Fracture surface area
Δt_m	Arbitrary unit time increment
$(\Delta A_R)_m$	Incremental increase in fracture surface area per unit time increment Δt_k

λ	Factor of proportionality
A_T	Total fractured area
A_d	Temporal fracturing area
R_d	Temporal fracturing radius based on Poiseuille's law
R_E	Temporal fracturing radius based on elastic model
R_V	Temporal fracturing radius based on asymptotic solutions (viscosity-dominated)
R_T	Temporal fracturing radius based on asymptotic solutions (toughness-dominated)
E	Young's modulus
E'	Plane strain Young's modulus
ν	Poisson's ratio
K_{IC}	Fracture toughness
K'	Reduced fracture toughness
k	Dimensionless fracture toughness
μ_f	Viscosity of fracturing fluid
μ'	Dynamic viscosity
Φ	Porosity
t	Time
t_{EXP}	Propagation duration of the hydraulic fracture in experiments
t_{mk}	Transition time required for fracture propagation from viscosity dominated to toughness dominated regimes
t_{om}	Characteristic time related to fluid lag to toughness dominated regimes
U	Compliance of injection system
χ	Time scale ratios of early-time initiation by compressibility of injection system to the late-time propagation under a constant injection Q_o
Ψ	Time scale ratios of fluid lag to the late-time propagation
C_o	Cohesion
σ_T	Tensile strength
σ_o	Confining stress or minimum horizontal stress
ϕ	Porosity
K	Permeability
$P(t)$	Wellbore pressure during injection time period
ζ	The Fraction of fluid within the hydraulic fracture
r	Cartesian coordinates x direction of a penny shaped fracture
z	Cartesian coordinates z direction of a penny shaped fracture
ξ	A dummy variable possessing same dimension with x
$U_z(r)$	The normal displacement of any point on upper part of crack disk

Reference

- Abé Ha, Keer L, Mura T (1976) Growth rate of a penny-shaped crack in hydraulic fracturing of rocks, 2. Journal of Geophysical Research 81:6292-6298
- Adachi J, Siebrits E, m, Peirce A, Desroches J (2007) Computer simulation of hydraulic fractures. International Journal of Rock Mechanics and Mining Sciences 44:739-757
- Advani S, Lee T, Lee J (1990) Three-dimensional modeling of hydraulic fractures in layered media: part I—finite element formulations
- Advani S, Torok J, Lee J, Choudhry S (1987) Explicit time-dependent solutions and numerical evaluations for penny-shaped hydraulic fracture models. Journal of Geophysical Research: Solid Earth 92:8049-8055
- Amitrano D (2003) Brittle-ductile transition and associated seismicity: Experimental and numerical studies and relationship with the b value. Journal of Geophysical Research: Solid Earth 108

- Batchelor CK, Batchelor G (2000) An introduction to fluid dynamics. Cambridge university press,
- Bunger AP (2005) Near-surface hydraulic fracture. University of Minnesota
- Bunger AP, Detournay E (2007) Early-time solution for a radial hydraulic fracture. *Journal of engineering mechanics* 133:534-540
- Bunger AP, Detournay E (2008) Experimental validation of the tip asymptotics for a fluid-driven crack. *Journal of the Mechanics and Physics of Solids* 56:3101-3115
- Bunger AP, Gordeliy E, Detournay E (2013) Comparison between laboratory experiments and coupled simulations of saucer-shaped hydraulic fractures in homogeneous brittle-elastic solids. *Journal of the Mechanics and Physics of Solids* 61:1636-1654
- Chen Z, Jeffrey RG, Zhang X, Kear J (2017) Finite-element simulation of a hydraulic fracture interacting with a natural fracture. *Spe Journal* 22:219-234
- Clifton RJ, Abou-Sayed AS A variational approach to the prediction of the three-dimensional geometry of hydraulic fractures. In: *SPE/DOE Low Permeability Gas Reservoirs Symposium*, 1981. OnePetro,
- Clifton RJ, Wang J-J Adaptive optimal mesh generator for hydraulic fracturing modeling. In: *The 32nd US Symposium on Rock Mechanics (USRMS)*, 1991. OnePetro,
- De Pater C, Cleary M, Quinn T, Barr D, Johnson D, Weijers L (1994a) Experimental verification of dimensional analysis for hydraulic fracturing. *SPE Production & Facilities* 9:230-238
- De Pater C, Weijers L, Savic M, Wolf K, Van Den Hoek P, Barr D (1994b) Experimental study of nonlinear effects in hydraulic fracture propagation (includes associated papers 29225 and 29687). *SPE Production & Facilities* 9:239-246
- Detournay E (2004) Propagation regimes of fluid-driven fractures in impermeable rocks. *International Journal of Geomechanics* 4:35-45
- Dontsov E (2016) An approximate solution for a penny-shaped hydraulic fracture that accounts for fracture toughness, fluid viscosity and leak-off. *Royal Society open science* 3:160737
- England A, Green A Some two-dimensional punch and crack problems in classical elasticity. In: *Mathematical Proceedings of the Cambridge Philosophical Society*, 1963. vol 2. Cambridge University Press, pp 489-500
- Feng R, Zhang Y, Rezagholilou A, Roshan H, Sarmadivaleh M (2020) Brittleness Index: from conventional to hydraulic fracturing energy model. *Rock Mechanics and Rock Engineering* 53:739-753
- Fung R, Vilayakumar S, Cormack DE (1987) Calculation of vertical fracture containment in layered formations. *SPE formation evaluation* 2:518-522
- Garagash D, Detournay E (2000) The tip region of a fluid-driven fracture in an elastic medium. *J Appl Mech* 67:183-192
- Garagash DI (2006) Propagation of a plane-strain hydraulic fracture with a fluid lag: Early-time solution. *International journal of solids and structures* 43:5811-5835
- Garagash DI Roughness-dominated hydraulic fracture propagation. In: *EOS Trans. AGU (Fall Meeting Suppl.)*, 2015. vol 52. pp MR41A-2628
- Garagash DI (2019) Cohesive-zone effects in hydraulic fracture propagation. *Journal of the Mechanics and Physics of Solids* 133:103727
- Geertsma J, De Klerk F (1969) A rapid method of predicting width and extent of hydraulically induced fractures. *Journal of petroleum technology* 21:1571-1581
- Green AE, Zerna W (1992) *Theoretical elasticity*. Courier Corporation,
- Holt RM, Fjær E, Stenebråten JF, Nes O-M (2015) Brittleness of shales: relevance to borehole collapse and hydraulic fracturing. *Journal of Petroleum Science and Engineering* 131:200-209
- Huang C, Chen S (2021) Effects of Ductility of Organic-Rich Shale on Hydraulic Fracturing: A Fully Coupled Extended-Finite-Element-Method Analysis Using a Modified Cohesive Zone Model. *SPE Journal* 26:591-609
- Kanaun S (2018) Efficient numerical solution of the hydraulic fracture problem for planar cracks. *International Journal of Engineering Science* 127:114-126
- Kanaun S (2020) On the hydraulic fracture of poroelastic media. *International Journal of Engineering Science* 155:103366

- Lecampion B, Desroches J (2015) Simultaneous initiation and growth of multiple radial hydraulic fractures from a horizontal wellbore. *Journal of the Mechanics and Physics of Solids* 82:235-258
- Lecampion B, Desroches J, Jeffrey RG, Bungler AP (2017) Experiments versus theory for the initiation and propagation of radial hydraulic fractures in low-permeability materials. *Journal of Geophysical Research: Solid Earth* 122:1239-1263
- Lecampion B, Detournay E (2007) An implicit algorithm for the propagation of a hydraulic fracture with a fluid lag. *Computer Methods in Applied Mechanics and Engineering* 196:4863-4880
- Legarth B, Huenges E, Zimmermann G (2005) Hydraulic fracturing in a sedimentary geothermal reservoir: Results and implications. *International Journal of Rock Mechanics and Mining Sciences* 42:1028-1041
- Lhomme T (2005) Initiation of hydraulic fractures in natural sandstones
- Liu D (2021) Hydraulic fracture growth in quasi-brittle materials. EPFL,
- Liu D, Lecampion B (2021) Propagation of a plane-strain hydraulic fracture accounting for a rough cohesive zone. *Journal of the Mechanics and Physics of Solids* 149:104322
- Nabipour A (2013) Experimental and numerical study of ultrasonic monitoring of hydraulic fracture propagation. Curtin University
- Naceur KB, Thiercelin M, Touboul E (1990) Simulation of fluid flow in hydraulic fracturing: implications for 3D propagation. *SPE production engineering* 5:133-141
- Nordgren R (1972) Propagation of a vertical hydraulic fracture. *Society of Petroleum Engineers Journal* 12:306-314
- Papanastasiou P, Papamichos E, Atkinson C (2016) On the risk of hydraulic fracturing in CO₂ geological storage. *International Journal for Numerical and Analytical Methods in Geomechanics* 40:1472-1484
- Peck D, Wrobel M, Perkowska M, Mishuris G (2018) Fluid velocity based simulation of hydraulic fracture: a penny shaped model—part I: the numerical algorithm. *Meccanica* 53:3615-3635
- Perkins T, Kern LR (1961) Widths of hydraulic fractures. *Journal of petroleum technology* 13:937-949
- Ranjith P, Viete DR, Chen BJ, Perera MSA (2012) Transformation plasticity and the effect of temperature on the mechanical behaviour of Hawkesbury sandstone at atmospheric pressure. *Engineering Geology* 151:120-127
- Rodriguez IV, Stanchits S (2017) Spatial and temporal variation of seismic attenuation during hydraulic fracturing of a sandstone block subjected to triaxial stress. *Journal of Geophysical Research: Solid Earth* 122:9012-9030
- Rybacki E, Reinicke A, Meier T, Makasi M, Dresen G (2015) What controls the mechanical properties of shale rocks?—Part I: Strength and Young's modulus. *Journal of Petroleum Science and Engineering* 135:702-722
- Sarmadivaleh M (2012) Experimental and numerical study of interaction of a pre-existing natural interface and an induced hydraulic fracture. Citeseer,
- Savitski A, Detournay E (2002) Propagation of a penny-shaped fluid-driven fracture in an impermeable rock: asymptotic solutions. *International journal of solids and structures* 39:6311-6337
- Shao S, Ranjith P, Wasantha P, Chen B (2015) Experimental and numerical studies on the mechanical behaviour of Australian Strathbogie granite at high temperatures: an application to geothermal energy. *Geothermics* 54:96-108
- Shapiro SA (2015) Fluid-induced seismicity. Cambridge University Press,
- Simonson E, Abou-Sayed A, Clifton R (1978) Containment of massive hydraulic fractures. *Society of Petroleum Engineers Journal* 18:27-32
- Sneddon I, Elliot H (1946) The opening of a Griffith crack under internal pressure. *Quarterly of Applied Mathematics* 4:262-267
- Sneddon IN (1946) The distribution of stress in the neighbourhood of a crack in an elastic solid. *Proceedings of the Royal Society of London Series A Mathematical and Physical Sciences* 187:229-260
- Sneddon IN (1995) Fourier transforms. Courier Corporation,

- Sarris E, Papanastasiou P (2011) The influence of the cohesive process zone in hydraulic fracturing modelling. *International Journal of Fracture* 167:33-45
- Valkó P, Economides MJ (1995) *Hydraulic fracture mechanics* vol 28. Wiley Chichester,
- van Dam DB, Papanastasiou P, De Pater C Impact of rock plasticity on hydraulic fracture propagation and closure. In: *SPE Annual Technical Conference and Exhibition*, 2000. OnePetro,
- Vandamme L, Curran J (1989) A three-dimensional hydraulic fracturing simulator. *International Journal for Numerical Methods in Engineering* 28:909-927
- Weinberg RF, Regenauer-Lieb K (2010) Ductile fractures and magma migration from source. *Geology* 38:363-366
- Wong T-f, Baud P (2012) The brittle-ductile transition in porous rock: A review. *Journal of Structural Geology* 44:25-53
- Zeng L, Reid N, Lu Y, Hossain MM, Saeedi A, Xie Q (2020) Effect of the fluid–shale interaction on salinity: implications for high-salinity flowback water during hydraulic fracturing in shales. *Energy & Fuels* 34:3031-3040
- Zhel'tov AK 3. Formation of vertical fractures by means of highly viscous liquid. In: *4th world petroleum congress*, 1955. OnePetro,
- Zhou D, Zhang G, Zhao P, Wang Y, Xu S (2018) Effects of post-instability induced by supercritical CO₂ phase change on fracture dynamic propagation. *Journal of Petroleum Science and Engineering* 162:358-366
- Zia H, Lecampion B (2020) PyFrac: A planar 3D hydraulic fracture simulator. *Computer Physics Communications* 255:107368